

# ***Downstream development of a detrital cooling-age signal: Insights from $^{40}\text{Ar}/^{39}\text{Ar}$ muscovite thermochronology in the Nepalese Himalaya***

**I.D. Brewer**

*Department of Geosciences, Pennsylvania State University, University Park, Pennsylvania 16802, USA*

**D.W. Burbank**

*Department of Earth Science, University of California, Santa Barbara, California 93106, USA*

**K.V. Hodges**

*Department of Earth, Atmospheric, and Planetary Sciences, Massachusetts Institute of Technology,  
Cambridge, Massachusetts 02139, USA*

## **ABSTRACT**

**The character and distribution of cooling ages in modern river sediment provide useful constraints on rates and patterns of uplift and erosion within actively deforming mountain ranges. Such sediment effectively samples all locations within the catchment area, irrespective of remoteness. We evaluate how successfully detrital cooling ages may be used to constrain hinterland erosion rates by examining the modern catchment of the Marsyandi River in central Nepal. Over the 100–200-km-length scale of the catchment, laser fusion  $^{40}\text{Ar}/^{39}\text{Ar}$  data for detrital muscovite collected from 12 separate sites illustrate the downstream development of a detrital cooling-age signal that is both systematic and representative of the contributing area. Comparisons of paired samples indicate that, at short spatial (tens of meters) and temporal (hundreds of years) scales, the detrital cooling-age signal is consistent. The distribution of bedrock cooling ages in a subcatchment and the resulting detrital signal at the catchment mouth can be modeled as a function of the erosion rate, relief, hypsometry, catchment area, and muscovite distribution. Given that independent constraints are available for most of these variables, the detrital age signal should be a robust indication of the spatially averaged erosion rate. In the Marsyandi, our model predicts erosion rate differences of approximately twofold, with higher rates (>2 mm/yr) along the southern topographic front of the Himalaya.**

**Keywords:** erosion rate, Himalaya, detrital ages, argon dating, Nepal.

## **INTRODUCTION**

In the absence of reliable temporal controls, rates of erosion, topographic evolution, and deformation during orogenic growth are poorly defined. Bedrock thermochronology is typically restricted to rocks currently exposed at the surface, where it provides a limited temporal record, because high ero-

sion rates in active orogens rapidly remove older rocks. Detrital mineral thermochronology, however, combines the antiquity of the stratigraphic record with the quantitative analysis of thermochronology (Bernet et al., 2001; Carrapa et al., 2003; Cervený et al., 1988; White et al., 2002). Because grab samples in a foreland basin contain millions of grains, each from a different point within the contributing catchment, detrital samples

provide a potent integration of orogenic data. When samples can be extracted from stratigraphic successions, detrital thermochronology provides the potential to document successive changes in the frequency of cooling ages and rates in an orogenic hinterland. Amid current controversy regarding thermal flux, and topographic steady state in orogens (Whipple, 2001; Willett and Brandon, 2002; Willett et al., 2001), detrital ages serve to define changes in lag times between mineral cooling and deposition—a key indicator of changing erosion rates or thermal state (Bernet et al., 2001; Bullen et al., 2003; Carrapa et al., 2003).

Before detrital thermochronological data can be reliably interpreted, however, the processes controlling the cooling-age signal need to be explored. Because a detrital sample represents an integration across a catchment, it is critical to know how the observed spectrum of detrital ages is influenced by patterns of erosion rate, variations in lithology, mechanical breakdown of grains during transport, and differences in sediment production and transport processes and rates (Spiegel et al., 2004). Due to practical limitations on the number of grain ages that can be measured, commonly only one sample is analyzed at a given stratigraphic level or point on a river system. Hence, the consistency of the detrital age signal should also be assessed: does it vary at spatial and temporal scales of tens of meters and hundreds of years?

Although the widest applicability of detrital age analyses may be to stratigraphic successions, many of the key controls are impossible to define in ancient catchments, e.g., spatial and temporal variations in erosion rate, lithology, source-area boundaries, topographic relief, and geomorphic processes. The hinterland may have been eroded away, and the boundaries of former catchments are almost always unknown. Consequently, modern catchments provide the best opportunity to explore the multiple variables that influence the detrital age signal carried to the foreland. Armed with such knowledge, and a good understanding of the possible uncertainties, interpretations of data from the rock record can be improved (Spiegel et al., 2004).

The distribution of bedrock cooling ages in a catchment can be modeled as a function of topographic relief, erosion rate, and the subsequent geothermal gradient (Mancktelow and Grasemann, 1997; Stüwe et al., 1994). For  $^{40}\text{Ar}/^{39}\text{Ar}$  dating of muscovite when the erosion rate is  $\leq 3$  mm/yr, the detrital cooling-age signal is determined by the hypsometry (the distribution of area with elevation) of the catchment (Brewer et al., 2003). These simple models, however, are applicable to catchments with spatially uniform erosion rates and homogeneous distributions of the target thermochronometer (in this case muscovite). In most active orogens, such restrictions would preclude the study of larger, orogenic-scale catchments and their foreland deposits.

In this study, we focus on the detrital system of the complete Marsyandi River, a trans-Himalayan river in central Nepal. We examine how the cooling-age signals of tributary catchments combine to produce a modern trunk-stream signal. We use  $^{40}\text{Ar}/^{39}\text{Ar}$  analysis of individual muscovite grains to examine

how the lithology, erosion rate, and hypsometry of individual catchment areas vary, and we investigate how these parameters control the evolution of the trunk-stream cooling-age signal as it travels downstream, from the headwaters to the foreland basin. This allows an examination of how well the cooling-age signal at the catchment mouth represents the contributing area upstream, and hence provides a baseline study for the interpretation of detrital ages preserved in the geological record.

The wide range in closure temperatures for different thermochronometers allows their application to many types of temperature-dependent geological problems. High-temperature thermochronometers are typically used to date the crystallization of minerals, whereas low-temperature thermochronometers are typically used to investigate late-stage cooling. The ages of detrital minerals have been used previously to assess provenance and source-area character (e.g., Adams et al., 1998; Garver and Brandon, 1994; Gehrels and Kapp, 1998), to estimate the age of the enclosing strata (e.g., Bullen et al., 2003; Carrapa et al., 2003; Garver et al., 1999; Najman et al., 2001), and to reconstruct orogenic cooling and erosion histories (e.g., Brandon and Vance, 1992; Copeland and Harrison, 1990; Spiegel et al., 2004; White et al., 2002).

Most of these previous investigations used sediments preserved in foreland basins, and despite the obvious value of the studies, interpretations can be ambiguous given the unknown variability in parameters, such as erosion rate, relief, and lithology, which modulate the detrital signal. Stock and Montgomery (1996) suggested that the range of detrital cooling ages in a particular catchment, in combination with a specified geothermal gradient, allows a theoretical calculation of catchment relief. Brewer et al. (2003) investigated how the interactions between geothermal gradient, erosion rate, and relief can be used in conjunction with the catchment hypsometry to predict the distribution of detrital cooling ages.

Although these studies (Stock and Montgomery, 1996; Brewer et al., 2003) reinforce the contention that detrital cooling-age data can provide useful tectonic-geomorphologic insights, they required uniform erosion rates across the catchment(s) of interest. Studies of detrital signals at the orogenic scale, however, should consider variable erosion rates, as well as variations in topography and lithology, because a large catchment produces a complex signal with detrital grains from multiple tributaries. In this paper, we build on previous work to investigate the parameters controlling the cooling-age signal from an entire orogenic-scale catchment. Field data from the Marsyandi Valley in central Nepal are used to examine the spatial pattern of erosion in the modern Himalaya.

## GEOLOGICAL BACKGROUND

The Himalaya represent a favorable study area for detrital age dating because the orogen encompasses stark contrasts in tectonic rates, erosion rates, lithology, and depth of exhumation. North of the Himalayan topographic axis, the Indus-Tsangpo

suture zone marks the surface boundary between lithologic units of Eurasian plate affinity to the north and Indian plate affinity to the south. After the initial collision at ca. 50–54 Ma (Rowley, 1996; Searle et al., 1997), the downgoing Indian plate was imbricated along a series of south-vergent thrust-fault systems, and the Himalaya formed as a result of the subsequent crustal thickening. Deformation continues today and global positioning system (GPS) data (Wang et al., 2001; Bilham et al., 1997) indicate that ~40% of the convergence between the Indian and Eurasian plates occurs across the Himalaya.

Thrust-fault systems mark many of the principal boundaries between tectonostratigraphic zones in the Himalaya. The Main Central thrust system juxtaposes high-grade metamorphic rocks and leucogranites of the Greater Himalayan sequence against lower-grade metasedimentary rocks of the Lesser Himalayan zone. Farther south, the Lesser Himalayan zone is separated from the foreland basin of the Himalaya by the Main Boundary thrust system. The topographic expression of the Indo-Asian collision closest to the foreland, the Siwalik Hills, corresponds to the Main Frontal thrust system. The initiation ages of these major thrust systems are progressively younger from north (22–28 Ma for the Main Central thrust system; Searle and Godin, 2003) to south (Pleistocene to Holocene for the Main Frontal thrust sys-

tem), although evidence exists for out-of-sequence thrusting along these and other less significant fault systems in the Himalayan realm over the Miocene-Holocene interval (Hodges, 2000; Wobus et al., 2003).

The surface trace of the Main Central thrust system marks the approximate physiographic transition from the Lesser to the Greater Himalaya, although in places this transition occurs >20 km south of the Main Central thrust (Wobus et al., 2003). The transition is marked by an abrupt increase in mean elevation and relief. As a consequence, much of the steep southern front of the Greater Himalaya, where erosion rates are likely to be more rapid, is developed on the metamorphic and igneous rocks of the Greater Himalayan sequence.

A fourth important fault system bounds the top of the Greater Himalayan sequence: the South Tibetan fault system. Carrying primarily unmetamorphosed, Neoproterozoic-Paleozoic clastic and carbonate sedimentary rocks of the Tibetan zone in its hanging wall, the South Tibetan fault system incorporates a variety of structures, but chief among them are low-angle, north-dipping detachments with normal-sense displacement (Burchfiel et al., 1992). In the study area, the South Tibetan fault system is composed of two primary splays: the Chame detachment and Machhapuchhare-Phu detachment (Fig. 1), which are commonly

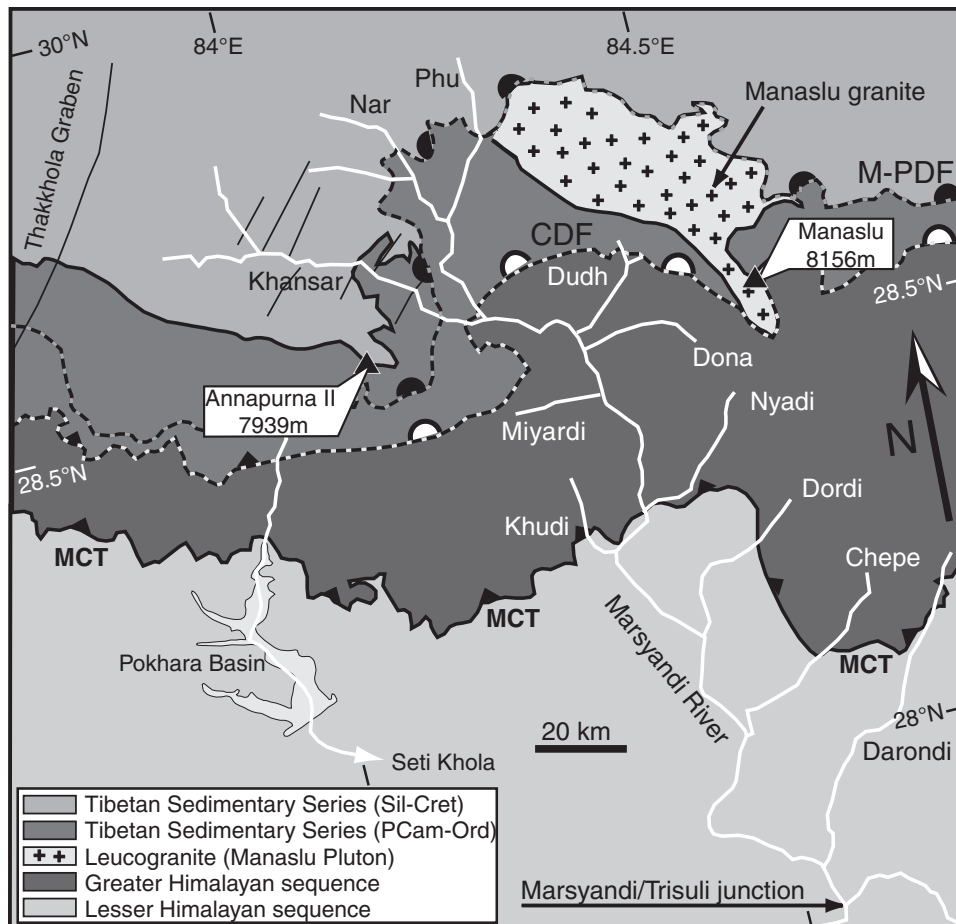


Figure 1. Simplified geological map of the Marsyandi region adapted from Searle and Godin (2003), Hodges et al. (1996), and Colchen (1986). The south-vergent Main Central thrust (MCT) separates the Greater Himalaya sequence from the Lesser Himalaya sequence. Other major south-vergent thrust faults, the Main Boundary thrust and the Main Frontal thrust, are to the south of this diagram. The South Tibetan fault system, with normal displacement, forms two splays in this region: the Chame detachment fault (CDF) and the Machhapuchhare-Phu detachment fault (MDF). Sil—Silurian; Cret—Cretaceous; PCam—Precambrian; Ord—Ordovician.

separated by the greenschist-to-amphibolite grade marble of the Annapurna Yellow Formation (Coleman, 1996; Hodges et al., 1996), although in the northeastern part of the study area, the Phu Detachment is interpreted to cut the top of the Manaslu pluton (Searle and Godin, 2003).

The Marsyandi River system of central Nepal (Fig. 1) has its headwaters north of the South Tibetan fault system and drains portions of the Tibetan, Greater Himalayan, and Lesser Himalayan zones over an area of  $\sim 4760$  km<sup>2</sup>. Its major tributaries flow over subsets of these tectonostratigraphic zones, and thus sediments in these tributaries sample different zones of bedrock. As they flow into the main Marsyandi trunk stream, individual tributary signals are progressively mixed downstream. The Khansar Khola (“khola” is the Nepali word for river) and Nar Khola predominately drain Tibetan zone sedimentary bedrock. The Dudh Khola drains Tibetan zone and Greater Himalayan rocks, as well as a major Miocene leucogranite, the Manaslu pluton (Le Fort, 1981). The Dona Khola drains this pluton, as well as a variety of metamorphic rocks of the Greater Himalayan sequence. The Miyardi and Nyadi Kholas have headwaters in the Greater Himalayan zone and exclusively sample this bedrock before emptying into the Marsyandi. The Khudi, Dordi, Chepe, and Darondi Kholas bridge the Main Central thrust system and thus have sediments with provenances in both the Greater and Lesser Himalayan sequences.

## METHODOLOGY

### Sampling Strategy

Detritus shed from a major mountain belt is primarily transported to the foreland basin by fluvial systems. En route, the development of the detrital age signal is influenced by the flux and composition of sediment contributed from tributaries. Thus, the foreland signal represents a complex integration of the dynamics of erosion and sediment transport in each tributary catchment. The sampling strategy in this investigation was designed to: (1) maximize the statistical robustness of cooling-age signals from individual tributaries; and (2) investigate the downstream development of the trunk-stream cooling-age signal; while (3) using small enough catchment areas to define adequately the spatial variation in cooling ages across this part of the orogen. With these objectives and given a finite number of laboratory age analyses, tradeoffs are unavoidable between obtaining the optimal representation of any single tributary, and reliably reconstructing the evolution of the detrital age signal along the course of the entire river. For example, a focus on small catchments will increase the resolution of spatial variation in bedrock cooling ages, but leaves fewer analyses to constrain the downstream evolution of the trunk stream. Conversely, more analyses on an individual sample will provide a more reliable characterization of the specific cooling-age signal, but limit the spatial resolution of the study.

Detrital sand samples were collected within the Marsyandi catchment from sites ranging from the Tibetan zone to the junction with the Trisuli River in the Lesser Himalayan zone (Fig. 2). At each sample site, large-grained sand was collected from bars within the modern river channel. Care was taken to avoid the influence of small tributaries and fill deposits, such as terraces, and to collect samples either upstream of sediment-mixing zones at river junctions or sufficiently below junctions ( $>1$  km) such that sediments could be considered well mixed by these turbulent rivers.

Although 27 samples were collected for point counting (to characterize the mineralogical constitution of the sediment), only 14 samples from twelve separate locations were selected for  $^{40}\text{Ar}/^{39}\text{Ar}$  dating. Six samples were chosen from the main stem of the Marsyandi River, and five samples were taken at

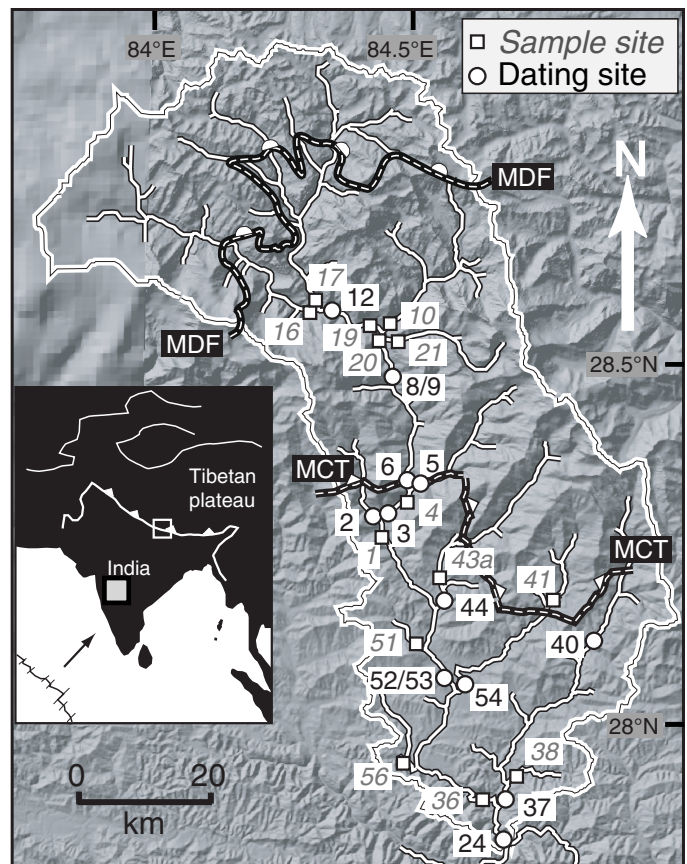


Figure 2. Map of Marsyandi catchment based on a 90 m digital elevation model (DEM). Sample locations are displayed with squares (and gray sample numbers) for point-counting sites and circles (and black sample numbers) for  $^{40}\text{Ar}/^{39}\text{Ar}$  analysis/point-count sites. The Marsyandi catchment (upstream of site 24) is outlined in white. The Main Central thrust (MCT) has triangles indicating south vergence, whereas the Machhapuchhare-Phu detachment fault (MDF) has half circles indicating extension down-to-the-north. The inset shows the approximate position of the sampling area within Central Asia and the modern geodetic Indo-Asian convergence rate (Wang et al., 2001).

the mouths of major tributaries (Fig. 2). One sample (S-40) represents a subcatchment within the overall Darondi Khola (S-37), taken to assess the relative input of ages from the Greater Himalayan sequence portion of the catchment in comparison to the entire catchment. To examine the temporal variability of the detrital signal, two samples were collected from the same location; one from the modern river bed (S-8), and one from a fill terrace elevated 2 m above it (S-9). To examine the natural spatial variability of the detrital signal, samples were collected 45 m apart on the downstream (S-53) and upstream (S-52) ends of the same sandbar. Samples S-8 and S-44 were reported in Brewer et al. (2003).

#### <sup>40</sup>Ar/<sup>39</sup>Ar Analytical Protocols

This investigation focused on detrital muscovite, which has been widely used in detrital mineral geochronology and appears to have fewer problems with excess argon than biotite (Roddick et al., 1980). Individual muscovite grains between 500–2000 μm were analyzed at the <sup>40</sup>Ar/<sup>39</sup>Ar laser microprobe facility at the Massachusetts Institute of Technology (Hodges, 1998). This grain size was used because, despite very rapid Himalayan erosion, it typically yields grains with sufficient radiogenic <sup>40</sup>Ar for reliable analysis. Hodges and Bowring (1995) provide additional details on the analytical techniques. Apparent ages calculated for each muscovite with an estimated 2σ uncertainty, obtained by propagating all analytical uncertainties, are available in the [Data Repository](#).<sup>1</sup>

Detrital cooling-age signals are commonly represented as probability density (PD) distributions, which represent the probability of finding a grain of a particular age, as a function of the age (Hurford et al., 1984; Silverman, 1986). Assuming that a Gaussian kernel represents the distribution of error (Brandon, 1996), a probability density function can be calculated for each grain, given the age ( $t_i$ ) and analytical uncertainty ( $\sigma$ ). For a sample of  $N$  grains collected from a specific locality, the probability density functions of individual grains ( $n$ ) can be combined:

$$P(t) = \sum_{n=1}^{n=N} \frac{1}{\sigma(n)\sqrt{2\pi}} e^{-\frac{(t-t_i(n))^2}{2\sigma(n)^2}} \quad (1)$$

By normalizing the area under the resulting curve to unity, a summed PD distribution is generated that represents the distribution of probability, as a function of age, within the sample.

#### Point Counting

Point counting of detrital samples serves two key purposes in this study. First, the abundance of muscovite in each tributary is a key ingredient in calculating how much the tributary contributes to the trunk-stream detrital age signal. Second, when detrital

minerals are used as conservative tracers, the relative abundance of a particular mineral species can define the relative contribution from individual tributaries. Although the latter technique has much lower resolution than the thermochronological approach, it provides an additional constraint on relative erosion rates.

Because of our emphasis on thermochronology, traditional point counting was primarily used to quantify the abundance of muscovite within the same 500–2000 μm fraction that was used for dating. Of the 600–900 grains counted in each sample, quartz, plagioclase, alkali feldspar, and micas were the major constituents counted, with additional minerals grouped together, and rock fragments considered to be an additional species. Crystalline carbonate was considered to be a mineral, whereas granular carbonate was considered a rock fragment. Rather than produce a very detailed description of the exact mineralogy in each sample (outside of the scope of this study), this broad approach provided an approximate quantification of major constituents (Table 1), which was sufficient for our modeling purposes. All reported errors from the point-counting results are taken from the statistical analysis of Van der Plas and Tobi (1965). To investigate the consistency of individual counts, repeat counts on three samples (S-1, S-2, S-3; Table 1) showed that the results were indistinguishable at the 2σ confidence level.

#### <sup>40</sup>Ar/<sup>39</sup>Ar RESULTS

Before attempting to interpret the <sup>40</sup>Ar/<sup>39</sup>Ar results using a modeling approach, the broad trends in the data illustrate a systematic downstream pattern in the trunk-stream age signal (Fig. 3). The catchment of the sample farthest upstream (S-12) drains the headwaters of the Marsyandi from the edge of the Tibetan Plateau to the crest of the Annapurna massif. The signal is dominated by an age population concentrated between 12 and 16 Ma. One source of these ages may be hydrothermal veins with <sup>40</sup>Ar/<sup>39</sup>Ar muscovite plateau dates of ca. 14 Ma that occur within Tibetan zone sedimentary rocks in this area (Coleman and Hodges, 1995). Alternatively, the catchment contains a small portion of the Annapurna Yellow Formation and the upper Greater Himalayan sequence, which may additionally contribute muscovite. The next sample downstream (S-8/S-9) was collected well south of the South Tibetan fault system and is influenced by two additional major tributaries, the Dudh and Dona Kholas, which drain the top of the Greater Himalaya sequence and Manaslu granite, and the Tibetan zone. Whereas the population of ages observed upstream (S-12) is still represented, the cooling-age signal is dominated by a major age population from 15 to 20 Ma. The weak expression of the younger than 15 Ma age population in the downstream sample and the paucity of muscovite (<1%; Table 1) in the upper reaches of the catchment suggest that the area upstream of sample S-12 (mostly Tibetan zone) makes

<sup>1</sup>GSA Data Repository item 2006027, Table DR1, Detrital <sup>39</sup>Ar/<sup>40</sup>Ar ages of muscovites from the Marsyandi River catchment, is available online at [www.geosociety.org/pubs/ft2006.htm](http://www.geosociety.org/pubs/ft2006.htm), or on request from [editing@geosociety.org](mailto:editing@geosociety.org) or Documents Secretary, GSA, P.O. Box 9140, Boulder, CO 80301, USA.

TABLE 1. POINT-COUNTING DATA FROM THE MARSYANDI VALLEY

Sample	Catchment	<i>n</i>	Qtz	Pl	Kfs	Ms	Bt	Frag	Opq	Other
S-1	Marsyandi	893	43.3 ±3.3	15.4 ±2.4	3.6 ±1.2	5.3 ±1.5	3.7 ±1.3	17.9 ±2.6	0.3 ±0.4	10.4 ±2.0
S-1.2	Marsyandi	798	45.6 ±3.5	14.7 ±2.5	4.6 ±1.5	6.5 ±1.7	4.0 ±1.4	18.5 ±2.8	0.1 ±0.2	5.9 ±1.7
S-2	Khudi	790	37.7 ±3.4	16.2 ±2.6	2.3 ±1.1	10.1 ±2.1	9.6 ±2.1	18.5 ±2.8	0.0 ±0.0	5.6 ±1.6
S-2.2	Khudi	765	42.7 ±3.6	19.6 ±2.9	2.1 ±1.0	11.9 ±2.3	11.2 ±2.3	7.4 ±1.9	0.2 ±0.3	4.3 ±1.5
S-3	Marsyandi	802	26.4 ±3.1	19.6 ±2.8	8.4 ±2.0	2.0 ±1.0	1.6 ±0.9	33.9 ±3.3	0.0 ±0.0	7.9 ±1.9
S-3.2	Marsyandi	800	30.3 ±3.2	15.8 ±2.6	10.0 ±2.1	2.6 ±1.1	2.4 ±1.1	35.3 ±3.4	0.1 ±0.2	3.4 ±1.3
S-4	Marsyandi	691	29.1 ±3.5	13.7 ±2.6	8.7 ±2.1	1.9 ±1.0	3.2 ±1.3	36.2 ±3.7	0.4 ±0.5	6.8 ±1.9
S-5	Nyadi	745	41.2 ±3.6	20.4 ±3.0	8.6 ±2.1	6.3 ±1.8	4.6 ±1.5	12.6 ±2.4	0.3 ±0.4	5.8 ±1.7
S-6	Marsyandi	779	27.3 ±3.2	17.1 ±2.7	9.6 ±2.1	3.5 ±1.3	2.6 ±1.1	35.6 ±3.4	0.8 ±0.6	3.6 ±1.3
S-8	Marsyandi	747	28.1 ±3.3	21.8 ±3.0	15.4 ±2.6	1.9 ±1.0	0.7 ±0.6	30.7 ±3.4	0.4 ±0.5	1.1 ±0.8
S-10	Dudh	804	40.2 ±3.5	29.9 ±3.2	16.0 ±2.6	1.7 ±0.9	0.0 ±0.0	9.3 ±2.1	0.1 ±0.2	2.7 ±1.1
S-16	Khansar	786	5.6 ±1.6	1.8 ±0.9	1.4 ±0.8	0.1 ±0.2	0.8 ±0.6	79.1 ±2.9	0.9 ±0.7	10.2 ±2.2
S-17	Nar	769	11.8 ±2.3	2.3 ±1.1	1.4 ±0.9	0.5 ±0.5	0.4 ±0.4	79.2 ±2.9	0.7 ±0.6	3.6 ±1.4
S-19	Marsyandi	784	15.9 ±2.6	14.0 ±2.5	7.5 ±1.9	1.8 ±0.9	2.0 ±1.0	53.6 ±3.6	0.6 ±0.6	4.5 ±1.5
S-20	Marsyandi	808	27.2 ±3.1	21.9 ±2.9	10.3 ±2.1	1.1 ±0.7	1.5 ±0.8	34.9 ±3.4	0.2 ±0.3	2.8 ±1.2
S-21	Dona	777	29.6 ±3.3	21.6 ±3.0	17.4 ±2.7	0.5 ±0.5	2.8 ±1.2	11.1 ±2.3	0.5 ±0.5	16.3 ±2.7
S-24	Marsyandi	768	49.1 ±3.6	9.1 ±2.1	3.1 ±1.3	6.8 ±1.8	3.9 ±1.4	23.4 ±3.1	0.5 ±0.5	3.9 ±1.4
S-36	Marsyandi	842	43.7 ±3.4	13.2 ±2.3	4.5 ±1.4	5.1 ±1.5	3.7 ±1.3	25.5 ±3.0	0.6 ±0.5	3.7 ±1.3
S-37	Darondi	869	62.7 ±3.3	13.1 ±2.3	1.2 ±0.7	4.6 ±1.4	2.9 ±1.1	12.5 ±2.2	1.0 ±0.7	1.8 ±0.9
S-38	LH trib	524	44.1 ±4.3	1.1 ±0.9	0.6 ±0.7	0.0 ±0.0	5.2 ±1.9	47.5 ±4.4	0.8 ±0.8	0.8 ±0.8
S-40	Darondi	624	55.8 ±4.0	13.3 ±2.7	0.6 ±0.6	7.2 ±2.1	3.8 ±1.5	13.8 ±2.8	0.5 ±0.6	4.5 ±1.7
S-41	Chepe	633	28.6 ±3.6	8.7 ±2.2	0.8 ±0.7	29.7 ±3.6	23.5 ±3.4	2.2 ±1.2	0.2 ±0.3	6.3 ±1.9
S-43a	Dordi	821	35.7 ±3.3	16.8 ±2.6	10.0 ±2.1	7.9 ±1.9	8.3 ±1.9	16.7 ±2.6	0.6 ±0.5	3.8 ±1.3
S-44	Dordi	777	43.8 ±3.6	14.3 ±2.5	2.7 ±1.2	9.7 ±2.1	9.1 ±2.1	12.6 ±2.4	1.4 ±0.8	6.4 ±1.8
S-51	LH trib	614	43.3 ±4.0	7.3 ±2.1	4.9 ±1.7	3.1 ±1.4	2.3 ±1.2	34.5 ±3.8	0.2 ±0.3	4.4 ±1.7
S-52	Marsyandi	858	31.6 ±3.2	13.6 ±2.3	5.5 ±1.6	10.6 ±2.1	11.0 ±2.1	22.5 ±2.9	0.5 ±0.5	4.8 ±1.5
S-53	Marsyandi	897	29.5 ±3.0	10.9 ±2.1	3.7 ±1.3	10.7 ±2.1	16.1 ±2.5	24.2 ±2.9	0.8 ±0.6	4.0 ±1.3
S-54	Chepe	884	40.4 ±3.3	9.3 ±2.0	2.1 ±1.0	23.2 ±2.8	11.9 ±2.2	7.3 ±1.8	0.3 ±0.4	5.4 ±1.5
S-56	LH trib	598	52.0 ±4.1	9.2 ±2.4	6.9 ±2.1	2.2 ±1.2	3.8 ±1.6	23.2 ±3.5	1.0 ±0.8	1.7 ±1.0

Note: Abbreviations: LH trib—Lesser Himalayan tributary; *n*—number of grains, Qtz—quartz, Pl—plagioclase, Kfs—potassium feldspar, Ms—muscovite, Bt—biotite, Frag—rock fragments, Opq—opaques, other—any other minerals. All errors are 2σ and are calculated with the statistical analysis of Van der Plas and Tobi (1965).

a minor volumetric contribution of muscovite when compared to other tributaries upstream of sample S-8/S-9.

Another 20 km farther downstream, the next trunk-stream sample (S-6) displays the same 15–20 Ma population seen in the upstream sample, but contains additional 5–15 Ma ages. After the Marsyandi crosses the Main Central thrust zone (S-3), the 0–10 Ma population becomes more dominant and the 15–20 Ma peak represents less than half the total probability. The growing downstream proportion of young cooling ages is clearly influenced by tributaries like Nyadi Khola (S-5), which drains the lower Greater Himalayan sequence and contains exclusively the 0–10 Ma age population. Additional downstream catchments contribute primarily 3–14 Ma ages, such that the lower Marsyandi River (S-52/S-53) shows a dominance of the 5–10 Ma age population after the influx of these tributaries.

In the Darondi Khola, a sample (S-40) collected above the Main Central thrust zone displays a clear 0–12 Ma population, whereas the sample (S-37) at the catchment mouth is similar, but includes a single older age component. Prior to merging with the Trisuli River, the trunk-stream Marsyandi sample (S-24) comprises a prominent 5–10 Ma signal, a lesser 10–15 Ma signal, and a weak 15–20 Ma signal.

## POINT-COUNTING RESULTS

The point-counting results (Table 1) indicate that the sediment composition changes systematically with the downstream addition of tributary material. Samples from the areally extensive Khansar and Nar catchments are rich in rock fragments containing up to 80%, mainly limestone, clasts from the Tibetan Sedimentary Series. The percentage of rock fragments in the tributaries rapidly decreases downstream, with some addition of granitic rock fragments, to between 20% and 30% toward the catchment mouth. The Dudh and Dona Kholas, draining the Manaslu granite, are quartz- and feldspar-rich and somewhat deficient in micas. The percentage of muscovite in the tributaries increases rapidly southward: Nyadi, Khudi, and Dordi Kholas all contain 5%–10% muscovite. Chepe Khola (S-54) has the largest fraction of muscovite, with nearly 30% (S-41) near the Main Central thrust (Fig. 2). This becomes diluted with the addition of quartz and rock fragments through the Lesser Himalaya, but remains over 20% at the catchment mouth. The Darondi Khola samples (S-37, S-40) show a similar trend of decreasing muscovite and increasing quartz through the Lesser Himalaya. The percentage of muscovite at the mouth of the Chepe, however, is ~4 times

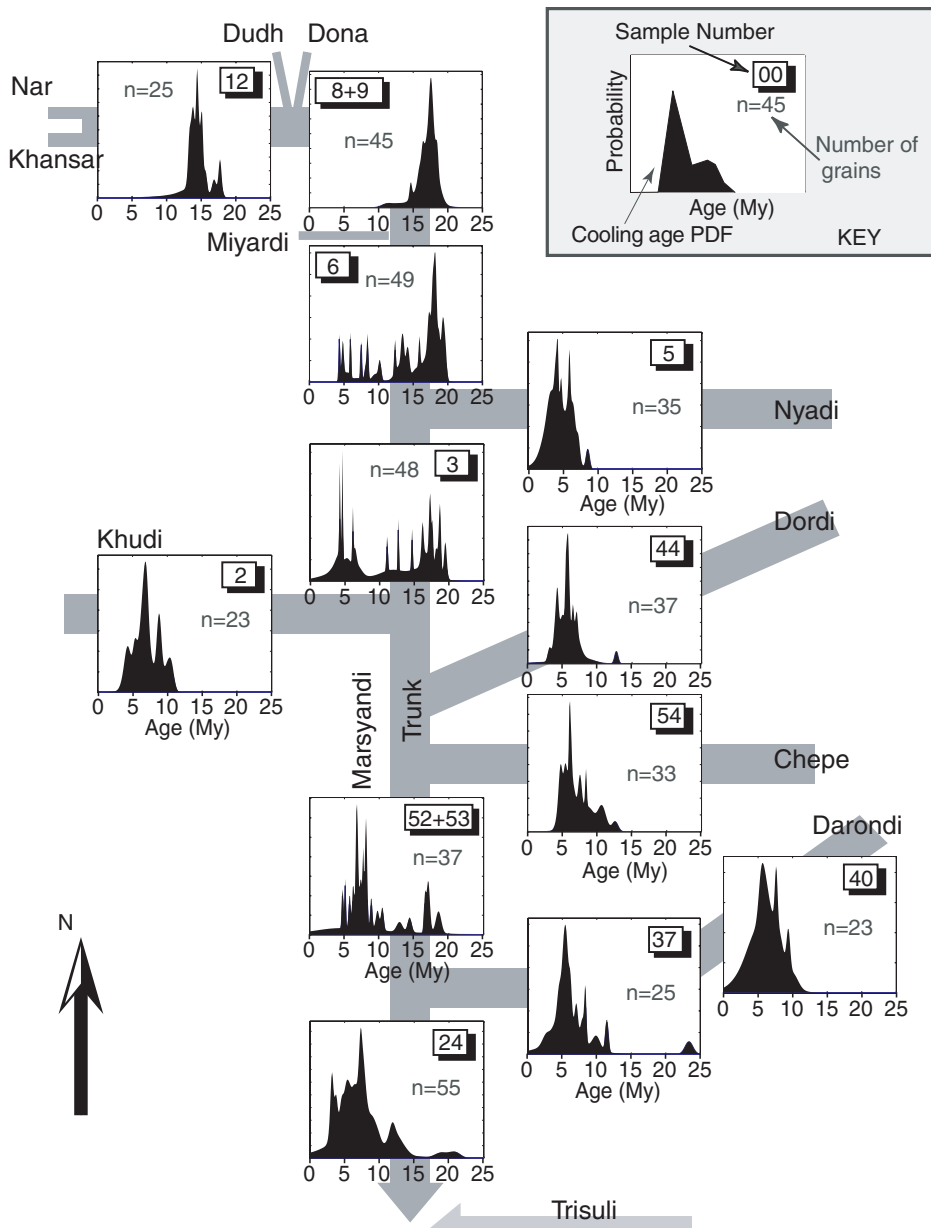


Figure 3. Detrital cooling-age probability density (PD) plots for samples from the Marsyandi catchment. All axes range from 0 to 25 m.y. on the x axis. Areas under the PD plot (shaded black) represent a total probability of one in each case, so that the probability scale on the y axis is relative. The individual plots have been arranged topologically to indicate their position within the Marsyandi River system: geographic locations are shown in Figure 2. Additional grain ages in sample 24 ( $229 \pm 18$  Ma) and sample 54 ( $27 \pm 0.9$  Ma) are not illustrated. PDF—probability density function.

greater than that at the mouth of the Darondi. Catchments contained wholly within Lesser Himalayan rocks (S-51, S-56, S-38) all show quartz contents of over 40%, high fractions of rock fragments, and muscovite abundances of 0%–3%. The high proportion of rock fragments may be a function of the immaturity of the sediment in relatively small catchments (S-38, S-51).

#### MODELING OF EROSION RATES AND SEDIMENT MIXING

Although the  $^{40}\text{Ar}/^{39}\text{Ar}$  analyses display systematic changes within the Marsyandi catchment, further insights into spatial variations in erosion (and perhaps tectonic) rates can be gained with numerical modeling. Such modeling allows us to examine

the impact of individual parameters (e.g., relief, hypsometry, lithology, and erosion rate) and discriminate between those characteristics of the data that can be explained by the model and those that cannot, forcing us to understand the limitations of initial assumptions. Thus, in combination with the  $^{40}\text{Ar}/^{39}\text{Ar}$  data, we use a numerical model to: (1) assess the spatial variation of parameters that control the hinterland cooling-age distributions; (2) understand how these parameters are manifested in the detrital cooling-age signal observed at the catchment mouth, and; (3) examine the reliability and resilience of the cooling-age signal.

To do this, we construct a theoretical PD distribution of cooling ages for each catchment within the Marsyandi drainage (Brewer et al., 2003). These PD distributions were generated by: (1) inputting the real topographic characteristics of each catch-

ment; and then (2) finding the optimal match between modeled and observed data PD distributions by varying the catchment erosion rate. Once theoretical PD distributions had been generated for each tributary, we modeled the relative contribution from each tributary to the trunk stream. Hence, we examined the systematic mixing of age populations in order to understand and predict the downstream evolution of the cooling-age signal within the Marsyandi Valley.

### Modeling the Detrital Cooling-Age Signal

Theoretical PD distributions had to be generated for each tributary. Firstly, to predict bedrock cooling ages within a tributary catchment, the predicted depth of the closure isotherm (at the time when muscovite passed through its closure temperature) was divided by the rate of erosion. Given a crust of predetermined thermal characteristics, the depth of the closure temperature is a function of the topographic relief and the rate of erosion. For erosion rates  $\leq 3$  mm/yr and topographic relief  $\leq 6$  km, the 350 °C closure isotherm of muscovite experiences negligible deflection due to surface topography (Mancktelow and Grasemann, 1997; Stüwe et al., 1994; Brewer et al., 2003). We used a simple thermal model (Brewer et al., 2003) to predict the depth of the closure isotherm as a function of catchment relief and erosion rate. The thermal model assumes vertical movement of rock toward the surface (given uniform surface heat flow [ $57 \times 10^{-3} \text{ Wm}^{-2}$ ], heat production [ $1.0 \times 10^{-6} \text{ Wm}^{-3}$ : Fowler, 1990], and conductivity) through a steady-state landscape containing hillslopes at a threshold for landsliding ( $\sim 30^\circ$  angle: Burbank et al., 1996). These assumptions produce a linear distribution of muscovite cooling ages with elevation. Given this, and with a uniformly eroding catchment, the cooling-age PD distribution is controlled by the distribution of land area with elevation, i.e., the hypsometry. Thus, the likelihood of sampling a particular age at the mouth of a catchment is predicted from the proportion of land containing that age.

In addition to the thermal and topographic parameters described in the preceding, the model required two further inputs: hypsometry and erosion rate. With this basic model, the larger Marsyandi Valley can be broken into individual catchments to represent the contribution from each of our tributary age samples. Given the hypsometry of a catchment, we modeled the cooling-age distribution as a function of the erosion rate. Because hypsometry can be extracted from a 90 m digital elevation model (DEM) for each catchment, the erosion rate was the only unknown parameter. Hence, the optimal model (with lowest mismatch between theoretical and observed PD distributions: Brewer et al., 2003) was found by varying the erosion rate within an individual catchment. Once the best model erosion rate for a tributary catchment had been found, we fixed it for subsequent analyses.

Ultimately, using all the tributaries, we wanted to predict how sediments from tributary catchments coalesce to form the trunk-stream signal. As a consequence of steady-state assumptions (that mean elevation and hypsometry are statistically invari-

ant over time scales exceeding 0.1 m.y.), the flux of material out of a catchment will balance the volume of rock moving into it. With vertical denudation for a unit time, the eroded volume is the product of the catchment area and the erosion rate. The progressive downstream summation of these products should model the evolving trunk-stream detrital signal.

If a mixing model were to rely solely on tributary area and erosion rate to predict relative contribution of muscovite to the trunk-stream detrital signal, a uniform distribution of muscovite must be assumed across the study area. In this study area, however, muscovite is heterogeneously distributed: it is common in high-grade metamorphic rocks, for example, but often absent in carbonates. Even within the high-grade rocks, muscovite shows 5-fold differences in abundance. Hence, the contribution from a carbonate catchment to the detrital muscovite age signal will be negligible, almost irrespective of its erosion rate. We used the percentage of muscovite at the mouth of each tributary, from the point-counting results (Table 1), to calculate a correction factor for the amount of muscovite per unit area present in each catchment (Fig. 4). Note that the percentage of muscovite varies over two orders of magnitude within the Marsyandi river system: any model that ignores a lithological correction factor here would yield profoundly biased results.

To model the trunk-stream signal at a particular location, we considered only the predetermined tributary PD distributions upstream of the sample. Our standard procedure (1) determined the erosion rate ( $dz/dt$ ) that optimized the fit with the observed data for each catchment given known relief and hypsometry (Table 2), and then (2) used the tributary area ( $A$ ) and abundance of muscovite ( $M_{\text{msc}}$ ) to calculate the relative contribution of the detrital signal from each tributary ( $PDF_A$  and  $PDF_B$ ) to the trunk-stream detrital signal ( $PDF_c$ ) downstream:

$$PDF_c = \frac{V_{\text{msc}_A}}{V_{\text{msc}_A} + V_{\text{msc}_B}} PDF_A = \frac{V_{\text{msc}_B}}{V_{\text{msc}_A} + V_{\text{msc}_B}} PDF_B, \quad (2)$$

where  $V_{\text{msc}}$  is the volume of muscovite supplied per unit time from a given tributary:

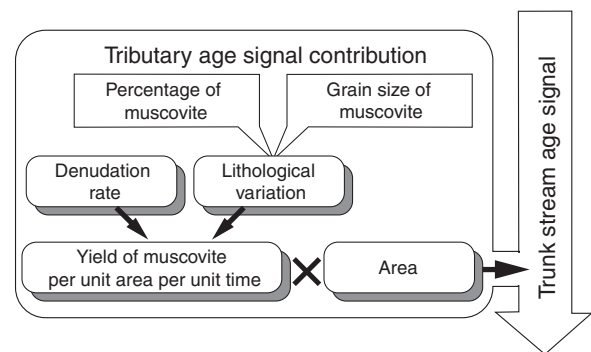


Figure 4. Parameters controlling the contribution of an individual tributary to a trunk-stream cooling-age signal. The foreland signal can be modeled as a specified mix of several such tributaries.

TABLE 2. TOPOGRAPHIC CHARACTERISTICS OF THE MARSYANDI VALLEY AND ITS ASSOCIATED TRIBUTARIES

Basin	Area (km <sup>2</sup> )	Elevation (m)				Lithology		
		Mean	Min	Max	Relief	~%TSS	~%GH	~%LH
Marsyandi	4760	3332	244	8152	7908			
Khansar	713	4794	2634	7824	5190	80	20	–
Nar	884	5209	2634	7097	4463	80	20	–
Dudh	392	4694	1958	7669	5711	10	90	–
Dona	129	4851	1895	8152	6257		100	–
Miyardi	60	4050	1496	5842	4346	–	100	–
Nyadi	215	3440	926	7495	6569	–	80	20
Khudi	136	2565	796	4914	4118	–	90	10
Dordi	351	2885	553	7756	7203	–	70	30
Chepe	309	1808	440	4872	4432	–	50	50
Darondi	609	1470	277	5787	5510	–	40	60

Note: The approximate litho-tectonic division of the basins are given in percentage area containing: Tethyan Sedimentary Series (TSS) structurally above the Machhapuchhare detachment fault; Greater Himalayan sequence (GH) complex, leucogranites, and Annapurna Yellow Formation; and Lesser Himalayan sequence (LH).

$$V_{msc} = \frac{dz}{dt} A M_{msc} \quad (3)$$

Although equation 2 describes mixing of two tributaries, when assessing the relative contribution of a tributary to the trunk stream (consisting of areas with different lithologies and erosion rates), we had to work progressively downstream, substituting the calculation of  $V_{msc}$  in a single tributary (equation 3) for the total volume of muscovite contributed per unit time from  $t$  tributaries upstream:

$$V_{msc} = \sum_{i=1}^n \frac{dz}{dt_i} A_i M_{msc_i} \quad (4)$$

Where tributary additions were unconstrained by ages at the tributary mouth (for example, the inaccessible area represented by the Miyardi Khola: Fig. 2), an erosion rate was assigned that was consistent with the surrounding tributaries and that minimized the mismatch of the trunk-stream signal in the sample directly below the junction. For the purposes of the modeling, the observed PD distributions were smoothed using a 2 m.y. scrolling window. This reduced the “peakedness” of the PD plots caused by individual grains, meaning that the calculated mismatch was less affected by individual grain peaks, but instead reflected the overall pattern of the entire signal.

### Modeling Results of PD Distributions

We previously described the results of modeling samples S-8 and S-44 (Brewer et al., 2003), and here we integrate these with the entire data set. The overall pattern of theoretical PD distributions that emerges from combining individual catchments (upstream Marsyandi, Nyadi, Khudi, Dordi, Chepe, and Darondi: Fig. 5) to produce the trunk-stream signal captures the primary age populations in the observed data. The main peaks of the theoretical plots generated for each tributary will align closely with

those of the data, because we minimized the mismatch by varying the erosion rate. The tails observed on either side of the younger peaks, however, are harder to match with our approach (i.e., see the Khudi Khola theoretical PD plot for illustration). The trunk stream displays a systematic pattern of change downstream as tributary signals are added. The >15 m.y. peak, prominent in the upstream samples, becomes diluted downstream as the 5–10 m.y. peak becomes increasingly important; although in comparison to the data, the predicted catchment mouth PD plot (as compared to S-24) is relatively depleted in the 10–15 m.y. age range.

In the upstream reaches of the Marsyandi, we had to modify our modeling procedure in order to find the best match to the observations. For our most upstream sample (S-12), draining the Nar and Khansar catchments (equal to one-third of the total Marsyandi catchment), the optimal erosion rate was modeled as ~1 mm/yr. By applying this rate to the entire upstream catchment area, the predicted flux to the upstream sample (S-12) produced a signal that, in comparison to the next downstream sample (S-8/S-9), was too dominant in the 10–15 m.y. age range. In order to reproduce the downstream observations, the relative contribution from the Nar and Khansar had to be reduced by ~50% compared to that indicated by the predicted erosion rate and the raw data for the percentage of muscovite (Table 1).

The reason for the initial mismatch is uncertain, but is likely a result in part of model assumptions that are violated in this catchment. First, we assumed that muscovite is uniformly distributed, whereas the lithologies of the catchment suggest that muscovite is more abundant in the southernmost part of the catchment that includes Greater Himalayan rocks (Searle and Godin, 2003). Second, we applied a uniform erosion rate to the entire catchment, whereas the lower relief and arid terrain in southern Tibet (north of the South Tibetan fault system) would be expected to erode more slowly than the wetter, higher relief part of the catchment underlain by Greater Himalayan rocks. Third, the point-count data from this catchment indicate a high fraction of rock fragments (~80%: Table 1), most of which are carbonates. This fraction rapidly decreases downstream through a reach with no major tributaries: a behavior suggesting that some combination of dissolution and mechanical breakdown is removing the carbonates from the sand fraction. Thus, the dominance of rock fragments makes estimates of muscovite abundance uncertain. Given these uncertainties in the appropriate flux, our decision to reduce the upstream contribution by 50% in order to match the observed downstream cooling ages seems permissible.

Although the model results mimic age distributions from tributaries with older cooling ages (i.e., the upstream catchments), they fail to reproduce the full range of ages in tributaries that yield younger cooling ages. The strong asymmetry observed in the older age tails is, in particular, difficult to replicate (the 8–13 Ma ages observed in the Chepe Khola, for example: Fig. 5). This mismatch may result from variations in erosion rate in the catchments to the south of the range crest, where rock uplift and erosion rates are expected to be locally controlled by the geometry of the active subsurface structure (e.g., Burbank et al.,

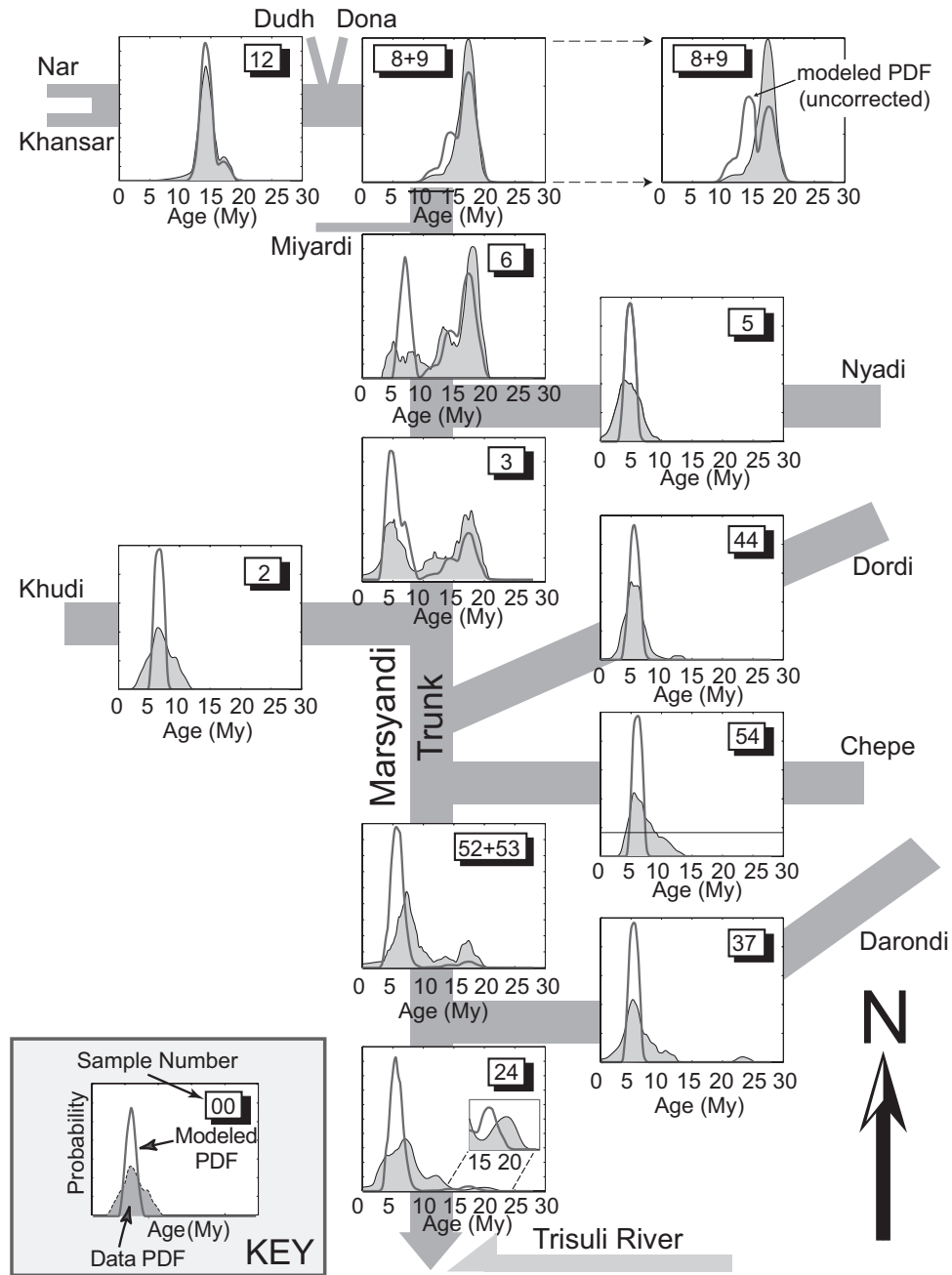


Figure 5. Model results compared to  $^{40}\text{Ar}/^{39}\text{Ar}$  analyses. Real-data probability density (PD) plots (identical to data used in Fig. 3) are shaded gray and smoothed using a 2 m.y. window. Solid black lines are model PD plots generated using the methodology described in the text and are also smoothed with a 2 m.y. window. The x axis of each plot ranges from 0 to 30 Ma, with probability on the y axis, and the area under each curve represents a probability of one. Inset for site S24 shows the 15–25 Ma observed age distributions (and theoretical curve) with a vertically exaggerated probability scale. Uncorrected theoretical PD plot for site S-8/S-9 is shown in the upper left. PDF—probability density function.

2003; Lavé and Avouac, 2001; Pandey et al., 1995; Seeber and Gornitz, 1983). In the absence of detailed tributary data or bedrock ages from these regions, however, we have limited the modeling to the same catchment resolution as our data. Another cause of mismatches would be areas not included in the modeling

(stippled in Fig. 6), yet contributing to the detrital cooling-age signal. There were insufficient thermochronological data from these areas to constrain their erosion rate. Most of these areas lie in the Lesser Himalaya, and if they have intermediate erosion rates, as their low relief and topography would suggest, then they

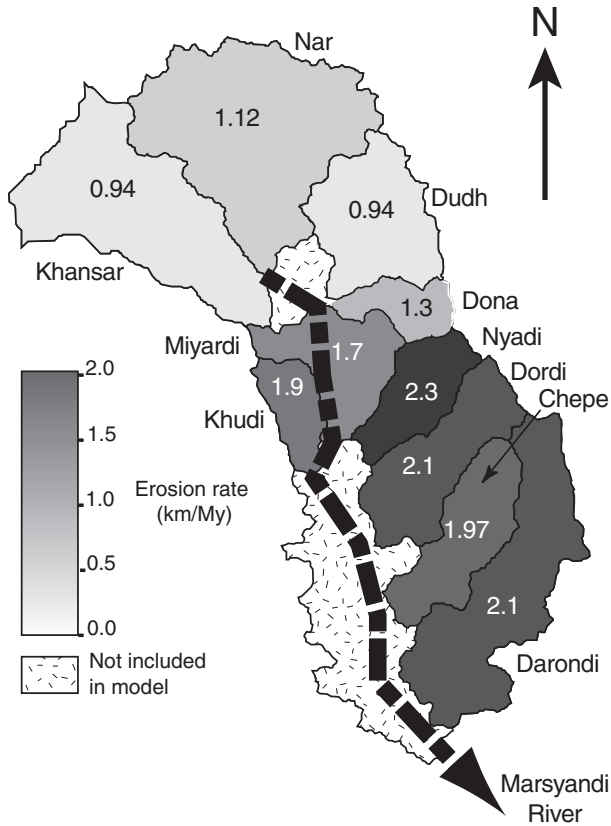


Figure 6. Spatial variation in erosion rates at the catchment scale. Erosion rates are taken from the results of modeling the detrital cooling-age probability density (PD) distributions for individual tributaries. The shaded areas indicate zones not included in the calculations and the dashed black line indicates the approximate path of the trunk stream. Highest erosion rates are predicted in the middle areas of the Marsyandi catchment, where rivers drain the steep front of the High Himalayas. Slowest erosion rates occur to the north of the topographic axis, in the rain shadow.

may be an additional source of 10–15 m.y. ages not represented in the model. Finally, our model assumes a topographic and thermal steady state since the time when rocks passed through the muscovite closure temperature, thereby implying steady erosion since closure. Whereas the model is insensitive to changes in erosion rate, such changes may have occurred. If rates have accelerated in the past 5 m.y. (Harrison et al., 1997; Wobus et al., 2003; Hodges et al., 2004), then older ages reflecting rocks that cooled prior to the onset of acceleration could be preserved at high elevations in a catchment, and hence preserve indications of slower erosion rates.

## DISCUSSION

The foregoing analysis makes numerous assumptions about controls on the observed cooling ages. For example, cooling is attributed simply to geomorphic erosion, and tectonic erosion by

extensional faulting is not considered. It is assumed that magmatic and fluid heating does not affect the observed cooling ages. Finally, folding or faulting since closure is assumed to have left the basic structure of the cooling ages unaffected.

Given the presence of a suite of normal faults, Miocene plutons, and active deformation in the study area, these assumptions need justification. Most previous studies of the South Tibetan fault system have concluded that the majority of slip occurred in the early Miocene and was completed by ca. 20 Ma (Burchfiel et al., 1992). More recently, Searle and Godin (2003) concluded that slip in the Marsyandi region was more recent than 19 Ma, but that most rapid cooling was complete by 15 Ma. In our study, the preponderance of observed ages are younger than 10 Ma, suggesting that extensional faulting has not been an important control on the muscovite cooling history. Similarly, emplacement of the Manaslu pluton at ca. 22–19 Ma (Harrison et al., 1995; Hodges et al., 1996) undoubtedly caused a thermal perturbation. Indeed, those detrital samples (S8, S9) that are most proximal to the Manaslu granite are dominated by 15–20 Ma muscovite ages (Fig. 3). Nonetheless, both upstream and downstream, cooling ages are much younger than this magmatic event and are deemed unaffected by it. We consider the possible effects of neofomed muscovites and hydrothermal heating to be small. In the vicinity of the Main Central thrust, brittle faulting (Hodges et al., 2004) and young cooling ages (Harrison et al., 1997; Wobus et al., 2003) suggest that deformation is ongoing. Quaternary displacements have been observed on at least one strand of the South Tibetan fault, but the associated rates of slip are low (Hurtado et al., 2001). Inevitably, some deformation has occurred since these rocks passed through their closure isotherm. The consistent pattern of young ages that is apparent south of the range crest (Figs. 3 and 5), however, suggests that deformation has not significantly offset the cooling ages when compared to the spatial scale of the Marsyandi Valley.

## Resilience of the Detrital Signal

One key concern with the application of detrital dating is the survivability of the target mineral(s) in the sediment routing system. If the river network causes rapid comminution of grains, a sample will only represent contributions of a small upstream area that is dependent on the rate of attrition. In our study such comminution would strongly influence the muscovite cooling-age signal that reaches the foreland, as information becomes progressively lost downstream. The ideal target thermochronometer is neither destroyed nor altered during the weathering and transportation history of the sediment, and should not be affected by postdepositional weathering or diagenesis.

Both chemical and physical processes may cause the breakdown of muscovite. Previous studies in Himachal Pradesh of Oligocene to lower Miocene Himalayan foreland strata (Najman et al., 1997), however, have indicated that chemical weathering has a negligible effect. Because we are studying a much younger Himalayan fluvial system, and because the Himalaya continues

to undergo rapid erosion with little storage of sediments within the hinterland, we assume that chemical alteration of muscovite does not significantly affect our results.

The process of physical attrition of muscovite grains during their passage through the fluvial system is more difficult to assess. With a hardness of 1–2 on Mohs scale and a well-developed basal cleavage, muscovite is susceptible to physical breakdown. However, muscovites do survive transport from the Himalaya to the distal Bengal Fan, a distance of >2000 km, with little disturbance of their  $^{40}\text{Ar}/^{39}\text{Ar}$  systematics (Copeland and Harrison, 1990). Given that the length scale of the Marsyandi catchment is an order of magnitude smaller, physical breakdown of muscovite is less likely to be significant. The persistence of the 15–20 Ma age signal from the upper Greater Himalaya sequence, through all our trunk-stream samples, lends support to this conclusion.

Rather than being a result of mechanical breakdown, we interpret the downstream decrease in the observed 15–20 Ma age signal to be an effect of dilution. Our modeling assumes a sediment flux proportional to the erosion rate and catchment size, but contains no function for the downstream loss of cooling-age signal with distance. Therefore, if comminution were significant over this length scale, the model would be expected to overrepresent the 15–20 m.y. age fraction, particularly in the lower reaches of the river as muscovite grains from upstream are increasingly destroyed. Instead, the model shows the opposite effect and points to dilution by detritus from more southerly catchments. We suggest that mica probably travels in the turbulent wash load of Himalayan rivers, where it experiences few grain-to-grain impacts and little downstream comminution.

Predicted cooling-age distributions are a function of erosion rate and the associated volume of eroded sediment per unit

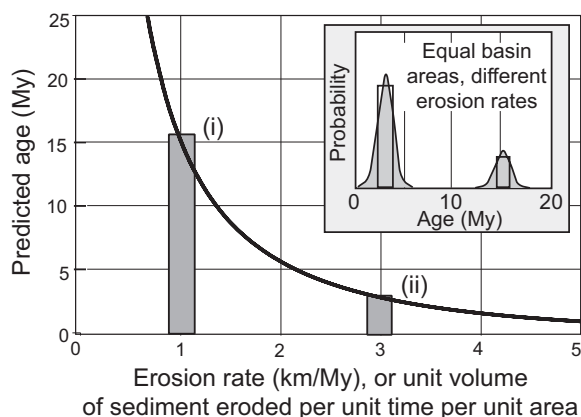


Figure 7. Predicted cooling ages from our model for specified erosion rates. The nonlinearity of the erosion rate–cooling age relation results from changes in the depth of the closure isotherm at different erosion rates. Relative abundances of detrital ages can be predicted based on erosion rates. For two catchments of equal area, but eroding at different rates [(i) 1 km/m.y.; (ii) 3 km/m.y.], 16 Ma cooling ages will constitute only 25% of the amalgamated age spectrum (inset).

area (Fig. 7). Thus, to investigate the relative proportion of an entire catchment that is producing a signal of a specific age, we need to correct for the volumetric contribution of that age. For example, although the 15–20 Ma age fraction in sample S-24 is relatively minor (Fig. 5), because it includes older cooling ages, it derives from an aeriially significant upstream area. Note that the relationship between predicted age and erosion rate (Fig. 7) is not linear in our model, because the depth of the closure isotherm varies as a function of denudation rate (Brewer et al., 2003). Reducing the erosion rate by a factor of two, from 2 to 1 mm/yr for example, has a large effect and changes the predicted cooling age threefold, from 5 to 15 m.y. (Fig. 7). In contrast, the exponential form of this curve means that, when comparing terrains producing cooling ages exceeding ~30 m.y., the difference between the volumetric contribution per unit area as a function of cooling age will be minor. In such cases, the probability distribution of age populations in the sediment will more closely reflect the size of the contributing areas.

### Reliability of the Cooling-Age Signal

Two important assumptions in detrital thermochronology studies are: (1) the sample is efficiently mixed during transportation; and (2) the signal is not prone to events that cause strong temporal variations in observed detrital ages. Landslides, rock falls, and localized storms could influence the latter. If these assumptions are correct, a grab sample should provide a reliable representation of the entire signal from the river and upstream catchment. Two pairs of samples were collected to investigate these assumptions.

The first pair addressed the homogeneity of fluvial mixing by examining the degree to which two samples varied within the modern river. Comparable results were produced by samples S-53 and S-52, which were collected ~45 m apart on the same sand bar in the trunk stream. To test if the age distributions from these two samples were statistically differentiable, we applied the Monte Carlo methodology as described by Brewer et al. (2003) to each observed population of ages to generate random grain ages, and then summed these ages to generate theoretical PD distributions. To represent the large range in errors seen in both our single-grain analyses and the summed PD distributions (Fig. 3), a more complex method of specifying the  $1\sigma$  analytical uncertainty was used for this approach. Because no consistent relationship of age uncertainty with grain age was observed (Fig. 8A), a PD plot was constructed of measured uncertainties (Fig. 8B). This error PD plot illustrates that, whereas most  $1\sigma$  analytical uncertainties are <1.5 m.y., larger errors are not uncommon. Therefore, for each modeled grain, the distribution of error ages (Fig. 8B) was randomly sampled (using the same Monte Carlo method), and the resultant  $1\sigma$  error was applied to the model-derived grain age.

Based on 500 individual grab samples randomly drawn from the modeled theoretical PD distribution for samples S-52/S-53 (Fig. 5), the calculated mismatch between the grab-sample

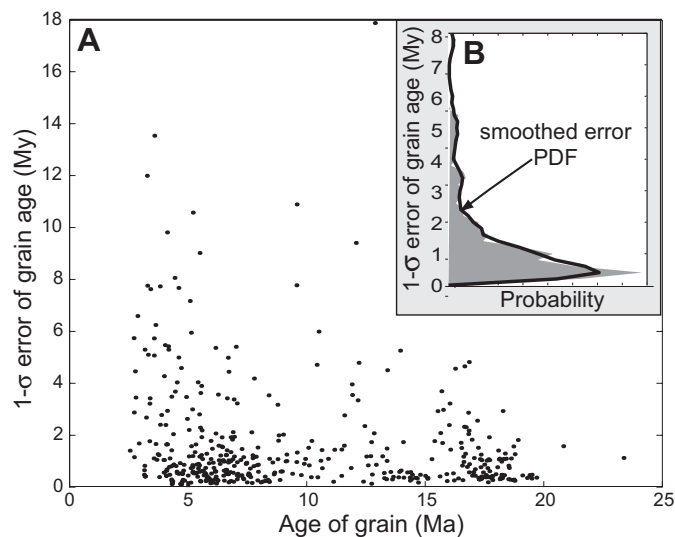


Figure 8. (A) Age versus error ( $1\sigma$ ) for analyses with greater than 40% radiogenic  $^{40}\text{Ar}$ . No clear relationship between age and error can be seen. Inset (B) shows a probability density function (PDF) plot generated from the  $1\sigma$  errors. This plot is smoothed (solid line) and used in the error determination in the numerical model. Based on this plot, most assigned errors will be between 0 and 1.5 m.y.

summed PD distribution and the theoretical PD distribution (Brewer et al., 2003) was compared against the observed mismatch between S-52 and S-53. A 2 m.y. smoothing window was again used before comparing curves to reduce the influence of individual grains. The theoretical modeling predicted a mismatch of  $\sim 20 \pm 14\%$  ( $2\sigma$ ), whereas the observed S-52/S-53 mismatch was 32% (Fig. 9). Hence, the observed mismatch of the two actual samples lies within the expected range of variability, and they cannot be proven to be statistically different from each other. Furthermore, in comparison to the observed sample mismatch, the theoretical mismatch is a minimum estimate, because it is drawn from a population defined by the observed samples, whereas the samples themselves were drawn from a broader age population.

The second pair of samples was collected from the modern river bed (S-8) and an adjacent terrace fill (S-9) to evaluate the temporal consistency of the detrital cooling-age signal at a particular location (Fig. 9B). Would samples that are separated by hundreds to thousands of years show the same age distribution? If not, the question of sediment storage and production becomes important. Large bedrock landslides, for example, might produce a pulse of sediment containing a restricted suite of ages. The same comparative procedure was applied to these samples, resulting in a 5% mismatch between S-8 and S-9 and an expected mismatch of  $21 \pm 15\%$  derived from the modeling. Thus the two PD distributions are very similar and cannot be considered statistically different. One caveat to this analysis, however, is that the almost unimodal cooling signal may mask temporal variability in sediment supply from this catchment area.

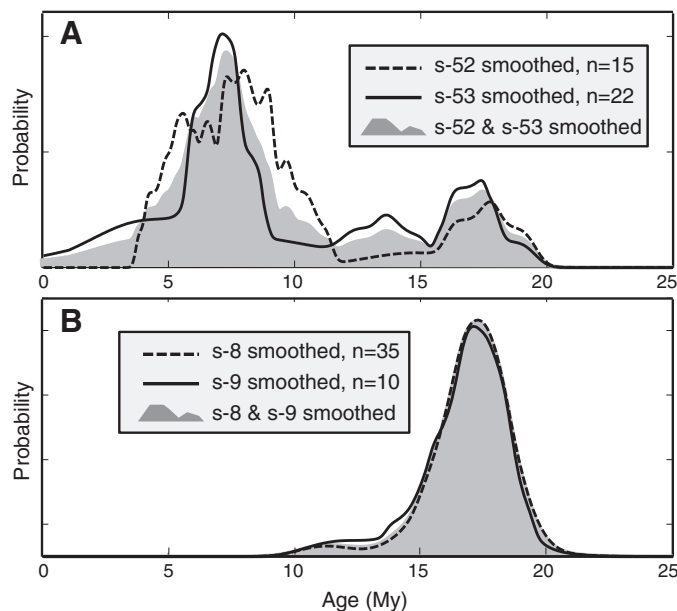


Figure 9. Results of repeat sampling to test (A) the spatial variability of the detrital cooling-age signal, and (B) the temporal variation of the signal. For each plot, the shaded probability density (PD) plot is the combined data used in the construction of Figure 5, while the PD plots represented by solid and dashed black lines are the contributing data. All curves are smoothed with a 2 m.y. scrolling window.

### Spatial Variations of Erosion Rate

Spatial variations in cooling ages derived from low-temperature thermochronology in orogenic belts are commonly used as proxies for analogous variations in erosion rates (e.g., Blythe et al., 2000; House et al., 2002). The results of our PD distribution modeling indicate that, within the Marsyandi catchment, erosion rates vary by more than twofold: from 0.9 to 2.3 km/m.y. (Fig. 6). The highest rates of 1.9–2.3 km/m.y. are found in catchments draining the topographic front of the Himalaya. Rates decrease to the north, with the Tibetan Sedimentary Series eroding at rates of 0.9–1.1 km/m.y. Areas to the south of the Main Central thrust probably have intermediate rates, but it is difficult to constrain the signal from solely the Lesser Himalaya, because most of the rivers also drain the Greater Himalaya sequence.

Consider the results from the Darondi Khola (Fig. 3). Approximately 40% of the catchment area lies above the Main Central thrust zone, as represented by sample S-40. At the catchment mouth, sample S-37 yielded similar ages to S-40, but drains the additional area of the Lesser Himalaya, which is 1.5 times the size of the Greater Himalaya part of the catchment. The similarity suggests that either: (1) the similar erosion rates prevail throughout the catchment; or (2) the Greater Himalaya sequence is producing most of the muscovite found at the catchment mouth. The latter could be explained either by

no effective erosion of the Lesser Himalaya sequence, or low percentages of muscovite in the Lesser Himalayan lithologies. Point counting suggests that the Greater Himalaya sequence is probably dominating the signal, because Lesser Himalayan catchments have low abundances of muscovite compared to those draining the Greater Himalayan sequence (Table 1). In addition, lower rates of erosion in the Lesser Himalaya, compared to higher rates on the topographic front, could be an explanation for the older PD distribution tails that are difficult to fit with the model for catchments draining both regions.

### Estimates of Relative Erosion Rates from Point-Counting Data

As defined by the point counting, the proportion of muscovite in the tributaries is used to scale each catchment flux in the PD distribution modeling described in the preceding sections. The complete mineral proportions of trunk stream and tributaries, however, may also be used for an additional calculation of erosion rate. Mixing the sediment of two rivers together should produce a resulting downstream sample that is representative of the relative contributions from each of the rivers. In reality, the natural variability of the fluvial system and point-counting errors mean that the data are not well resolved. Because of this uncertainty, we use a basic model to examine the general pattern of contributions from each of the inputs and resulting mixing within the trunk stream.

The model uses point-counting data from each of the upstream samples and mixes them to produce a resulting downstream signal. The contribution of each upstream sample is varied from 0% to 100%, and the best solution is picked by finding the minimum residual to the downstream sample. This procedure assumes ideal mixing and no selective deposition or attrition of individual mineral species. We have already suggested that the carbonate rock fragments are susceptible to comminution and dissolution, and hence in some areas, they will bias the ratios. Therefore, we found that, instead of (1) mixing all the species at once; or (2) dropping out problematic individual mineral species and recalculating the mixing ratio (with or without renormalizing), the most consistent results were obtained by solving for the optimal mixing ratio ( $\phi_j$ ) for the observed concentration ( $M$ ) of each mineral species ( $j$ ) individually in the upstream trunk ( $a$ ) and catchment ( $b$ ) samples and downstream ( $c$ ) samples:

$$[M_{j_c}] = \phi_j [M_{j_a}] + (1 - \phi_j) [M_{j_b}] \quad (5)$$

and then calculating the mean mixing ratio ( $\bar{\phi}$ ) for the number of species point counted ( $n$ ) in the sample:

$$\bar{\phi} = \frac{1}{n} \sum_{j=1}^n \phi_j \quad (6)$$

This procedure weighted each mineral species equally, eliminating instances where individual mineral species controlled the mixing ratio due to their large volume (e.g., quartz).

Given mean mixing ratios ( $\bar{\phi}$ ) and catchment areas ( $A$ ), relative erosion rates ( $dz/dt_{rel}$ ) for individual tributaries within the Marsyandi were then calculated (Fig. 10):

$$\frac{dz}{dt_{relb}} = \frac{\bar{\phi} V_a}{(1 - \bar{\phi}) A_b} \quad (7)$$

To use this approach to examine the relative mixing of two tributaries, the volume ( $V_a$ ) of material contributed per unit time in tributary a needs to be known. Thus, initially the relative erosion rates in the two most upstream tributaries were determined, assuming an arbitrary erosion rate of 1 unit per unit time in tributary a. Subsequently, as a function of area,  $V_a$  was calculated:

$$V_a = A_a \frac{dz}{dt_{rela}} \quad (8)$$

Moving systematically downstream, relative erosion rates (compared to that of tributary a) of downstream tributaries can be calculated, such that the relative rate of tributary b is calculated with tributary a representing the upstream trunk-stream sample (equation 7), and  $V_a$  is calculated assuming that the total contributed volume per unit time of the trunk stream is a summation of  $t$  tributary inputs upstream:

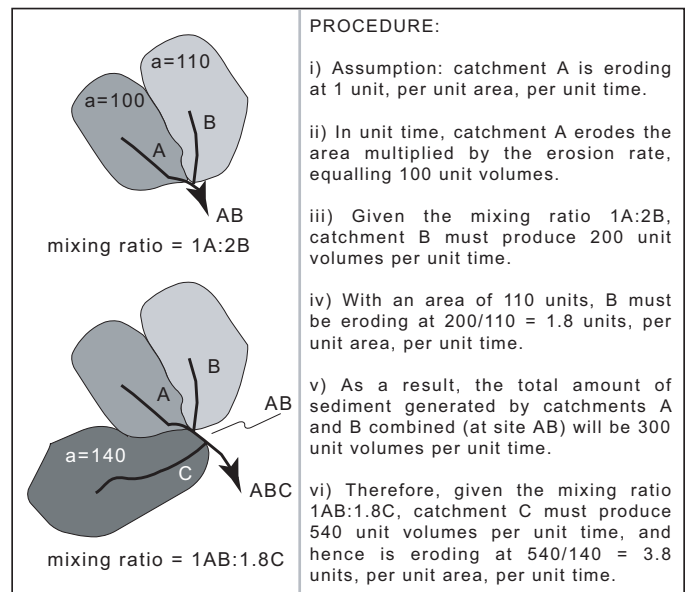


Figure 10. The procedure used to convert point-counting results into relative erosion rates. Point counting of sediment samples from the mouth of catchment A and the mouth of catchment B, in conjunction with a downstream sample AB, can be used to calculate a mixing ratio for the two catchments. When combined with catchment area, extracted from a digital elevation model, this ratio is used to calculate a relative erosion rate.

$$V_a = \sum_{i=1}^t A_i \frac{dz}{dt_{rel_i}} \quad (9)$$

Finally, we rescaled the relative erosion rate in the Dordi catchment to match the erosion rate determined from cooling ages in the same catchment, and then applied this same rescaling factor to all other catchments. This was solely done to provide relative erosion-rate estimates (Fig. 11) in magnitudes that could be easily compared to those calculated using thermochronology (Fig. 6).

Although clear differences appear between the erosion rates calculated from thermochronology (Fig. 6) and those calculated from the point-counting analysis (Fig. 11), the general pattern of low erosion in the north of the region, high erosion rates in catchments on the southern flank of the main topographic axis, and intermediate erosion rates to the south, is the same. Whereas the PD distribution modeling suggested variations in erosion rate

of up to 2.5-fold, the point-counting model yielded variations in predicted rates more than tenfold. These discrepancies are not surprising due to the expected variability of sediment within the river: (1) species such as rock fragments will become comminuted downstream; (2) carbonate rock fragments and minerals will experience chemical, as well as physical, erosion; and (3) hydraulic sorting will be important for minerals with different densities, although sorting appears to have little impact on muscovite in the 500–2000  $\mu\text{m}$  size range, as shown by samples S-52 and S-53 (Fig. 9).

## CONCLUSIONS

Through examination of the downstream development of a detrital mineral cooling-age signal, this investigation provides insights into long-standing questions concerning the interpretation of detrital mineral ages. In the past, a sample collected from the foreland basin might be used to interpret erosion rates in the upstream catchment area, but where the erosion was occurring and how much of the catchment it represented remained unknown. Here, we show that there are systematic and predictable changes in the detrital cooling-age signal of a large, transverse Himalayan river. For example, large regions of a catchment may contribute little to the foreland signal if they are either eroding slowly or have a low abundance of the mineral, such as muscovite, that is being dated.

Our analysis of the Marsyandi Valley catchment detrital system yields insights on how the inputs from tributary catchments combine to form the signal at the catchment mouth. By implementing a thermal-erosional numerical model, we can use the cooling-age distributions from individual tributaries and observable characteristics of the catchment (relief and hypsometry) to determine a best-fit erosion rate. More typically, erosion rates have been estimated using individual bedrock cooling ages or suites of samples in vertical relief profiles (e.g., Blythe et al., 2000; Bullen et al., 2003; House et al., 2002; Ehlers and Farley, 2003). Because detrital samples can yield dozens to hundreds of cooling ages from throughout a catchment, when combined with catchment hypsometry and a thermal model, they provide a potentially potent tool for estimating erosion rates (Brewer et al., 2003; Bernet et al., 2004a).

The numerical modeling indicates that the detrital cooling-age signal changes systematically in the trunk stream, whereby the input of an age population from an individual tributary is a function of the abundance per unit area of the thermochronometer, the area of the catchment, and the rate at which it is eroding. As seen in other studies (Bernet et al., 2004a, 2004b), our mixing model for detrital ages was more successful in matching the central ages of observed cooling-age populations than in reproducing the relative abundance of those populations (Fig. 5). Previous studies have suggested that the failure to match relative abundances may be unavoidable because of the natural unsteadiness in fluvial systems (Bernet et al., 2004a). We are more optimistic, but suggest that the use of larger numbers of

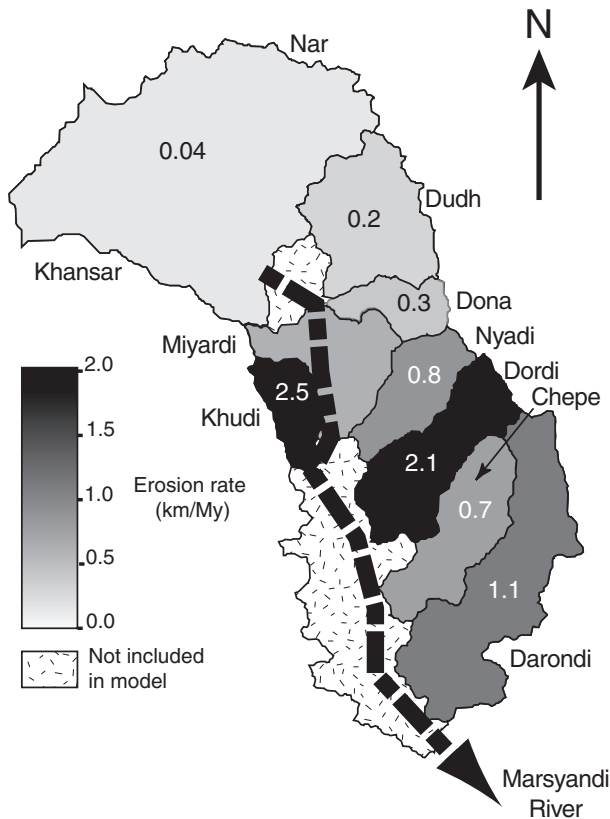


Figure 11. Spatial variation in erosion rates at the catchment scale based on point-counting data (Table 1) using the methodology illustrated in Figure 10. Relative erosion rates are normalized by the Dordi Khola to allow direct comparison with those derived from the cooling ages (Fig. 6). The stippled areas indicate zones not included in the calculations, and the dashed black line indicates the approximate path of the trunk stream. Note that the overall pattern of erosion is similar to that predicted from cooling ages, with high erosion rates in the middle areas of the Marsyandi catchment and slowest erosion rates to the north of the topographic axis.

ages (>80 for complex age distributions), smaller catchments (across which erosion rates are more likely to be constant), thorough sampling (all important tributary catchments), and better statistics on mineral abundances should underpin significant improvement in this approach.

In our analysis, the distribution of muscovite is a critical factor in determining the representation of a particular area of the catchment in the foreland sample. For example, ~30% of the Marsyandi catchment is composed of the Tethyan Sedimentary Series, and yet these strata produce only a small fraction of the foreland detrital cooling-age signal because of the paucity of muscovite within these strata. Most previous detrital dating studies that examined downstream mixing (e.g., Bernet et al., 2004b) assumed that the mineral being dated had a uniform areal distribution at the scale of the catchments being compared. The ~100-fold variation in muscovite abundance documented here suggests that this assumption needs to be evaluated in almost all studies where heterolithic distributions of rocks can be expected. Whereas examination of geologic maps may provide insights on the spatial distributions of rock types (Bernet et al., 2004b), the comparative fraction of the target mineral needs to be measured for calibration when relative fluxes are calculated.

Comparison of the detrital age data versus modeling results indicates that comminution of muscovite by fluvial processes seems to be insignificant at the 100–200 km scale (within the 500–2000  $\mu\text{m}$  analytical size range used). The 15–20 Ma signal derived from the Marsyandi headwaters is persistent downstream, although it decreases in significance. We argue that the calculated volumes of muscovite added to the trunk stream are consistent with the downstream dilution of this signal by younger age populations, rather than mechanical breakdown of muscovite. The absence of significant mica loss may be attributable to muscovite moving in suspended load during the monsoon season, thus encountering less abrasion than during bedload transportation.

In detrital studies, the reproducibility of detrital age samples needs to be assessed. Here, we evaluated samples from (1) different sites on the same sandbar and (2) from nearby deposits of different ages and showed that the detrital cooling-age signal appeared spatially and temporally reliable in this area. A recent study of the consistency of fission-track ages in detrital samples from the Rhone delta (Bernet et al., 2004b) also concluded that, within a  $2\sigma$  uncertainty, the same component age peaks were represented in all samples. Such tests are recommended for other modern detrital studies.

The results of the thermochronometry suggest that the topographic front of the Himalaya is eroding faster than regions north and south of it. In particular, those catchments draining the Greater Himalayan sequence are generating abundant ca. 4–10 Ma cooling ages that appear to reflect erosion rates exceeding ~2 mm/yr. Areas to the north of the Himalayan topographic axis, on the edge of the Tibetan Plateau, experience the lowest erosion rates and produce grain ages between 10 and 15 Ma for those catchments sourced in the Tibetan zone, and 15–20 Ma for those catchments draining the top of the Greater Himalayan

sequence and the Manaslu granite. Intermediate rates are probably found in the Lesser Himalaya, although the large tributaries draining this zone have headwaters in, and cooling-age signals dominated by, the Greater Himalaya. The pattern of erosion from thermochronology is broadly consistent with the erosion rates calculated from point-counting data. The latter predicts a greater contrast in the erosion rates that should be interpreted cautiously, however, because of the intrinsic variability of sediments within the river system.

Several Himalayan tectonic interpretations can be compared with the south-to-north increase in erosion rates predicted by this study. First, if the Main Central thrust and South Tibetan fault system are active, high erosion rates of the Greater Himalaya might be expected with the southward extrusion of the Greater Himalaya sequence (Beaumont et al., 2001; Hodges et al., 2001). Such extrusion predicts highest erosion rates toward the middle part of the Greater Himalaya, about halfway between the South Tibetan fault and the Main Central thrust (Beaumont et al., 2001). Our data cannot rule this out, but appear more consistent with rapid erosion in the vicinity of the Main Central thrust. Similarly, our study's gradient in erosion across the Greater Himalaya is inconsistent with the interpretation of uniform erosion across the Greater Himalaya that emerges from apatite fission-track studies, which show uniformly young ages spanning the Greater Himalaya (Burbank et al., 2003). Alternatively, the gradient of increased erosion rates toward the south is consistent with either an active Main Central thrust or a shift of the deformation front a few tens of kilometers into the Main Central thrust footwall (Harrison et al., 1997; Wobus et al., 2003).

Any of these tectonic interpretations introduces the complicating factor of lateral advection. In most investigations to date, cooling ages are converted into rock exhumation rates using an assumption of one-dimensional thermal and kinematic processes. For instance, in our model, the depth of the closure isotherm varies as a function of erosion rate and topographic relief, but rock particles still move vertically toward the surface. The thermal structure of an active convergent orogen is not particularly well represented by a simple model of horizontal isotherms, because it is subject to the lateral advection of heat into the orogen (e.g., Batt and Braun, 1997; Jamieson and Beaumont, 1988; Jamieson et al., 1998; Willett, 1999), and rock particles move laterally, not solely vertically, during erosion. Although beyond the scope of this paper, this complicating factor needs to be considered when evaluating our results.

This baseline investigation illustrates that, when assessed with the array of samples from within the Marsyandi catchment, the downstream evolution of the detrital cooling-age signal in the trunk stream is consistent. It can be numerically modeled as a function of contributions from tributaries with variable erosion rates, areas, relief, hypsometries, and muscovite abundances. The detailed interpretation of the most downstream (or foreland) sample by itself, however, is complex because of the patterns of tributary mixing and differential erosion. For example, the foreland sample is dominated by a 4–10 Ma population of grain ages,

and one might argue that the southern catchments (the Nyadi Khola and downstream), which represent ~40% of the area sampled, control the signal. On closer inspection, however, cooling ages from these catchments cannot explain all the intricacies of the older signal: the upstream catchments that drain the upper Greater Himalayan rocks and Tibetan Sedimentary Series, representing ~55% of the catchment area, are needed to account for the 15–20 Ma age population (Figs. 2 and 5). Our modeling suggests that, despite a larger contributing area, this upstream signal is so much less dominant in the foreland due to the effects of volumetric contribution: catchment lithology and erosion rate.

In this study, we have dated ~500 muscovite grains from 12 locations, providing new insights into how lithology and catchment characteristics, both easily observable in other modern locations, influence the detrital age signal of the Marsyandi River. Although we agree that the distribution of cooling ages within the foreland provides useful information about the range of erosion rates in the hinterland, considerable caution is needed when interpreting the source and importance of detrital age populations from stratigraphic samples. The ability to confidently relate modern detrital age samples to hinterland cooling and erosion patterns (Bernet et al., 2001) is not easily duplicated in the past (Spiegel et al., 2004). Yet in order to extract the maximum amount of information from the stratigraphic record, an understanding of analogous but commonly unknown parameters (hypsometry, catchment area, lithology, erosion rate) that control the cooling-age signal is vital. An appreciation for both for the complexity of interactions in modern detrital systems, and for the primary controls on the detrital age signal, will support improved interpretations of the spatial and temporal evolution of orogens based on detrital age studies in the ancient stratigraphic record.

## ACKNOWLEDGMENTS

We thank P. DeCelles, M. Brandon, M. Bernet, and an anonymous reviewer for their incisive comments. Advice and assistance from R. Slingerland, K. Furlong, M. Bullen, W. Olszewski, J. Hurtado, A. White, and M. Krol significantly improved this analysis. Logistical assistance in Nepal was provided by Himalayan Experience. This research was supported by National Science Foundation grants to Burbank (EAR-9627865, 9896048, 9909647) and by grants from the Chevron Corporation and the Krynine Fund to Brewer.

## REFERENCES CITED

- Adams, C.J., Barley, M.E., Fletcher, I.R., and Pickard, A.L., 1998, Evidence from U-Pb zircon and  $^{40}\text{Ar}/^{39}\text{Ar}$  muscovite detrital mineral ages in metasediments for movement of the Torlesse suspect terrane around the eastern margin of Gondwanaland: *Terra Nova*, v. 10, p. 183–189, doi: 10.1046/j.1365-3121.1998.00186.x.
- Batt, G., and Braun, J., 1997, On the thermomechanical evolution of compressional orogens: *Geophysical Journal International*, v. 128, p. 364–382.
- Beaumont, C., Jamieson, R.A., Nguyen, M.H., and Lee, B., 2001, Himalayan tectonics explained by extrusion of a low-viscosity crustal channel coupled to focused surface denudation: *Nature*, v. 414, p. 738–742, doi: 10.1038/414738a.
- Bernet, M., Zattin, M., Garver, J.I., Brandon, M.T., and Vance, J.A., 2001, Steady-state exhumation of the European Alps: *Geology*, v. 29, no. 1, p. 35–38, doi: 10.1130/0091-7613(2001)029<0035:SSEOTE>2.0.CO;2.
- Bernet, M., Brandon, M.T., Garver, J.I., and Molitor, B.R., 2004a, Fundamentals of detrital zircon fission-track analysis for provenance and exhumation studies with examples from the European Alps, in Bernet, M., and Spiegel, C., eds., *Detrital thermochronology: Geological Society of America Special Paper 378*, p. 25–36.
- Bernet, M., Brandon, M.T., Garver, J.I., and Molitor, B., 2004b, Downstream changes of Alpine zircon fission-track ages in the Rhône and Rhine Rivers: *Journal of Sedimentary Research*, v. 74, p. 82–94.
- Bilham, R., Larson, K., Freymueller, J., and Project Idylhim members, 1997, GPS measurements of present-day convergence across the Nepal Himalaya: *Nature*, v. 386, p. 61–64.
- Blythe, A.E., Burbank, D.W., Farley, K.A., and Fielding, E.J., 2000, Structural and topographic evolution of the central Transverse Ranges, California, from apatite fission-track, (U-Th)/He and digital elevation model analysis: *Basin Research*, v. 12, p. 97–114, doi: 10.1046/j.1365-2117.2000.00116.x.
- Brandon, M.T., 1996, Probability density plot for fission-track grain-age samples: *Radiation Measurements*, v. 26, p. 663–676, doi: 10.1016/S1350-4487(97)82880-6.
- Brandon, M.T., and Vance, J.A., 1992, Fission-track ages of detrital zircon grains: Implications for the tectonic evolution of the Cenozoic Olympic subduction complex: *American Journal of Science*, v. 292, p. 565–636.
- Brewer, I.D., Burbank, D.W., and Hodges, K.V., 2003, Modelling detrital cooling-age populations: Insights from two Himalayan catchments: *Basin Research*, v. 15, p. 305–320, doi: 10.1046/j.1365-2117.2003.00211.x.
- Bullen, M.E., Burbank, D.W., and Garver, J.I., 2003, Building the northern Tien Shan: Integrated thermal, structural, and topographic constraints: *Journal of Geology*, v. 111, p. 149–165, doi: 10.1086/345840.
- Burbank, D.W., Leland, J., Fielding, E., Anderson, R.S., Brozovic, N., Reid, M.R., and Duncan, C., 1996, Bedrock incision, rock uplift and threshold hillslopes in the northwestern Himalayas: *Nature*, v. 379, p. 505–510, doi: 10.1038/379505a0.
- Burbank, D.W., Blythe, A.E., Putkonen, J., Pratt-Sitaula, B., Gabet, E., Oskin, M., Barros, A., and Ojha, T.P., 2003, Decoupling of erosion and precipitation in the Himalayas: *Nature*, v. 426, p. 652–655, doi: 10.1038/nature02187.
- Burchfiel, B.D., Zhileng, C., Hodges, K.V., Yuping, L., Royden, L.H., Changrong, D., and Jiene, X., 1992, The South Tibetan detachment system, Himalayan orogen: Extension contemporaneous with and parallel to shortening in a collisional mountain belt: *Geological Society of America Special Paper 269*, 41 p.
- Carrapa, B., Wijbrans, J., and Bertotti, G., 2003, Episodic exhumation in the Western Alps: *Geology*, v. 31, no. 7, p. 601–604, doi: 10.1130/0091-7613(2003)031<0601:EEITWA>2.0.CO;2.
- Cerveny, P.F., Naeser, N.D., Zeitler, P.K., Naeser, C.W., and Johnson, N.M., 1988, History of uplift and relief of the Himalaya during the past 18 million years; evidence from sandstones of the Siwalik Group, in Kleinspehn, K.L., and Paola, C., eds., *New perspectives in basin analysis: New York, Springer-Verlag*, p. 43–61.
- Colchen, M., LeFort, P., and Pêcher, A., 1986, *Annapurna–Manaslu–Ganesh Himal*: Paris, Centre National de la Recherche Scientifique, 136 p.
- Coleman, M.E., 1996, The tectonic evolution of the central Himalaya, Marsyandi Valley, Nepal [Ph.D. thesis]: Boston, Massachusetts Institute of Technology, 221 p.
- Coleman, M.E., and Hodges, K.V., 1995, Evidence for Tibetan Plateau uplift before 14 Myr ago from a new minimum age for east-west extension: *Nature*, v. 374, p. 49–52, doi: 10.1038/374049a0.
- Copeland, P., and Harrison, M.T., 1990, Episodic rapid uplift in the Himalaya revealed by  $^{40}\text{Ar}/^{39}\text{Ar}$  analysis of detrital K-feldspar and muscovite, Bengal Fan: *Geology*, v. 18, p. 354–359, doi: 10.1130/0091-7613(1990)018<0354:ERUITH>2.3.CO;2.
- Ehlers, T.A., and Farley, K.A., 2003, Apatite (U-Th)/He thermochronometry: Methods and applications to problems in tectonic and surface processes: *Earth and Planetary Science Letters*, v. 206, p. 1–14, doi: 10.1016/S0012-821X(02)01069-5.
- Fowler, C.M.R., 1990, *The solid Earth: An introduction to geophysics*: Cambridge, Cambridge University Press, 490 p.
- Garver, J.I., and Brandon, M.T., 1994, Fission-track ages of detrital zircons from Cretaceous strata, southern British Columbia: Implications

- for the Baja BC hypothesis: *Tectonics*, v. 13, no. 2, p. 401–420, doi: 10.1029/93TC02939.
- Garver, J.I., Brandon, M.T., Roden-Tice, M., and Kamp, P.J.J., 1999, Exhumation history of orogenic highlands determined by detrital fission-track thermochronology, in Ring, U., Brandon, M.T., Willett, S., and Lister, G., eds., *Exhumation processes: Normal faulting, ductile flow, and erosion*: Geological Society Special Publication 154, p. 283–304.
- Gehrels, G.E., and Kapp, P.A., 1998, Detrital zircon geochronology and regional correlation of metasedimentary rocks in the Coast Mountains, southeastern Alaska: *Canadian Journal of Earth Sciences*, v. 35, p. 269–279, doi: 10.1139/cjes-35-3-269.
- Harrison, T.M., McKeegan, K.D., and LeFort, P., 1995, Detection of inherited monazite in the Manaslu leucogranite by  $^{208}\text{Pb}/^{232}\text{Th}$  ion microprobe dating: crystallization age and tectonic implications: *Earth and Planetary Science Letters*, v. 133, p. 271–282, doi: 10.1016/0012-821X(95)00091-P.
- Harrison, T.M., Ryerson, F.J., Le Fort, P., Yin, A., Lovera, O.M., and Catlos, E.J., 1997, A late Miocene-Pliocene origin for the central Himalayan inverted metamorphism: *Earth and Planetary Science Letters*, v. 146, p. E1–E7, doi: 10.1016/S0012-821X(96)00215-4.
- Hodges, K.V., 1998,  $^{40}\text{Ar}/^{39}\text{Ar}$  thermochronology using the laser microprobe, in McKibben, M.A., and Shanks, W.C., eds., *Applications of microanalytical techniques to understanding mineralizing processes*: Society of Economic Geologists Reviews in Economic Geology, v. 7, p. 53–72.
- Hodges, K.V., 2000, Tectonics of the Himalaya and southern Tibet from two perspectives: *Geological Society of America Bulletin*, v. 112, p. 324–350, doi: 10.1130/0016-7606(2000)112<324:TOTHAS>2.3.CO;2.
- Hodges, K.V., and Bowring, S., 1995,  $^{40}\text{Ar}/^{39}\text{Ar}$  thermochronology of isotopically zoned micas: Insights from the southwestern USA Proterozoic orogen: *Geochimica et Cosmochimica Acta*, v. 59, p. 3205–3220, doi: 10.1016/0016-7037(95)00209-1.
- Hodges, K.V., Parrish, R.R., and Searle, M.P., 1996, Tectonic evolution of the central Annapurna Range: Nepalese Himalayas: *Tectonics*, v. 15, p. 1264–1291, doi: 10.1029/96TC01791.
- Hodges, K.V., Hurtado, J.M., and Whipple, K.X., 2001, Southward extrusion of Tibetan crust and its effect on Himalayan tectonics: *Tectonics*, v. 20, p. 799–809, doi: 10.1029/2001TC001281.
- Hodges, K.V., Wobus, C., Ruhl, K., Schildgen, T., and Whipple, K., 2004, Quaternary deformation, river steepening, and heavy precipitation at the front of the Higher Himalayan ranges: *Earth and Planetary Science Letters*, v. 220, p. 379–389, doi: 10.1016/S0012-821X(04)00063-9.
- House, M.A., Gurnis, M., Kamp, P.J.J., and Sutherland, R., 2002, Uplift in the Fiordland region, New Zealand: Implications for incipient subduction: *Science*, v. 297, p. 2038–2041, doi: 10.1126/science.1075328.
- Hurford, A.J., Fitch, F.J., and Clarke, A., 1984, Resolution of the age structure of the detrital zircon populations of two Lower Cretaceous sandstones from the Weald of England by fission track dating: *Geological Magazine*, v. 121, p. 269–277.
- Hurtado, J.M., Jr., Hodges, K.V., and Whipple, K., 2001, Neotectonics of the Thakkhola Graben and implications for recent activity on the South Tibetan fault system in the central Nepal Himalaya: *Geological Society of America Bulletin*, v. 113, no. 2, p. 222–240, doi: 10.1130/0016-7606(2001)113<0222:NOTTGA>2.0.CO;2.
- Jamieson, R.A., and Beaumont, C., 1988, Orogeny and metamorphism; a model for deformation and pressure-temperature-time paths with applications to the Central and Southern Appalachians: *Tectonics*, v. 7, p. 417–445.
- Jamieson, R.A., Beaumont, C., Fullsack, P., and Lee, B., 1998, Barrovian regional metamorphism: Where's the heat, in Treloar, P.J., and O'Brien, P.J., eds., *What drives metamorphism and metamorphic reactions*: Geological Society [London] Special Publication 138, p. 23–51.
- Lavé, J., and Avouac, J.P., 2001, Fluvial incision and tectonic uplift across the Himalaya of Central Nepal: *Journal of Geophysical Research*, v. 106, p. 26,561–26,591, doi: 10.1029/2001JB000359.
- Le Fort, P., 1981, Manaslu leucogranite: A collision signature in the Himalaya, a model for its genesis and emplacement: *Journal of Geophysical Research*, v. 86, p. 10,545–10,568.
- Mancktelow, N.S., and Grasemann, B., 1997, Time-dependent effects of heat advection and topography on cooling histories during erosion: *Tectonophysics*, v. 270, p. 167–195, doi: 10.1016/S0040-1951(96)00279-X.
- Najman, Y., Pringle, M., Godin, L., and Oliver, G., 2001, Dating of the oldest continental sediments from the Himalayan foreland basin: *Nature*, v. 410, p. 194–197, doi: 10.1038/35065577.
- Najman, Y.M.R., Pringle, M.S., Johnson, M.R.W., Robertson, A.H.F., and Wijbrans, J.R., 1997, Laser  $^{40}\text{Ar}/^{39}\text{Ar}$  dating of single detrital muscovite grains from early foreland-basin sedimentary deposits in India: Implications for early Himalayan erosion: *Geology*, v. 25, p. 535–538, doi: 10.1130/0091-7613(1997)025<0535:LAADOS>2.3.CO;2.
- Pandey, M.R., Tandukar, R.P., Avouac, J.P., Lavé, J., and Massot, J.P., 1995, Interseismic strain accumulation on the Himalayan crustal ramp (Nepal): *Geophysical Research Letters*, v. 22, no. 7, p. 751–754, doi: 10.1029/94GL02971.
- Roddick, J., Cliff, R., and Rex, D., 1980, The evolution of excess argon in Alpine biotites—A  $^{40}\text{Ar}/^{39}\text{Ar}$  analysis: *Earth and Planetary Science Letters*, v. 48, p. 185–208, doi: 10.1016/0012-821X(80)90181-8.
- Rowley, D.B., 1996, Age of initiation of collision between India and Asia: A review of stratigraphic data: *Earth and Planetary Science Letters*, v. 145, p. 1–13, doi: 10.1016/S0012-821X(96)00201-4.
- Searle, M.P., and Godin, L., 2003, The South Tibetan detachment and the Manaslu leucogranite: A structural reinterpretation and restoration of the Annapurna-Manaslu Himalaya, Nepal: *Journal of Geology*, v. 111, p. 505–523, doi: 10.1086/376763.
- Searle, M.P., Corfield, C., Stephenson, B., and McCarron, J., 1997, Structure of the North Indian continental margin in the Ladakh-Zaskar Himalayas: Implications for the timing of obduction of the Spontang ophiolite, India-Asia collision and deformation events in the Himalaya: *Geological Magazine*, v. 134, p. 297–316, doi: 10.1017/S0016756897006857.
- Seeber, L., and Gornitz, V., 1983, River profiles along the Himalayan arc as indicators of active tectonics: *Tectonophysics*, v. 92, p. 335–367, doi: 10.1016/0040-1951(83)90201-9.
- Silverman, B.W., 1986, *Density estimation for statistics and data analysis*: London, Chapman and Hall, 175 p.
- Spiegel, C., Siebel, W., Kuhlemann, J., and Frisch, W., 2004, Toward a comprehensive provenance analysis: A multi-method approach and its implications for the evolution of the Central Alps, in Bernet, M., and Spiegel, C., ed., *Detrital thermochronology—Provenance analysis, exhumation, and landscape evolution of mountain belts*: Geological Society of America Special Paper 378, p. 37–50.
- Stock, J.D., and Montgomery, D.R., 1996, Estimating palaeorelief from detrital mineral age ranges: *Basin Research*, v. 8, no. 3, p. 317–328.
- Stüwe, K., White, L., and Brown, R., 1994, The influence of eroding topography on steady-state isotherms: Application to fission track analysis: *Earth and Planetary Science Letters*, v. 124, p. 63–74, doi: 10.1016/0012-821X(94)00068-9.
- Van der Plas, L., and Tobi, A.C., 1965, A chart for judging the reliability of point counting results: *American Journal of Science*, v. 263, p. 87–90.
- Wang, Q., Zhang, P.-Z., Freymueller, J.T., Bilham, R., Larson, K.M., Lai, X.A., You, X., Niu, Z., Jianchun, W., Li, Y., Liu, J., and Yang, Z., 2001, Present-day crustal deformation in China constrained by global positioning system measurements: *Science*, v. 294, p. 574–577.
- Whipple, K.X., 2001, Fluvial landscape response time; how plausible is steady-state denudation?: *American Journal of Science*, v. 301, p. 313–325.
- White, N.M., Pringle, M., Garzanti, E., Bickle, M., Najman, Y., Chapman, H., and Friend, P., 2002, Constraints on the exhumation and erosion of the High Himalayan Slab, NW India, from foreland basin deposits: *Earth and Planetary Science Letters*, v. 195, p. 29–44, doi: 10.1016/S0012-821X(01)00565-9.
- Willett, S.D., 1999, Orogeny and orography: The effects of erosion on the structure of mountain belts: *Journal of Geophysical Research*, v. 104, p. 28,957–28,982, doi: 10.1029/1999JB900248.
- Willett, S.D., and Brandon, M.T., 2002, On steady states in mountain belts: *Geology*, v. 30, no. 2, p. 175–178, doi: 10.1130/0091-7613(2002)030<0175:OSSIMB>2.0.CO;2.
- Willett, S.D., Slingerland, R., and Hovius, N., 2001, Uplift, shortening, and steady state topography in active mountain belts: *American Journal of Science*, v. 301, no. 4–5, p. 455–485.
- Wobus, C.W., Hodges, K.V., and Whipple, K.X., 2003, Has focused denudation sustained active thrusting at the Himalayan topographic front?: *Geology*, v. 31, p. 861–864, doi: 10.1130/G19730.1.